TU Delft

Delft University of Technology

Ductile fracture assessment of wire and arc additive manufactured steel materials

Xin, Haohui; Li, Junqiang; Zhang, Youyou; Veljkovic, Milan; Persem, Nicolas; Lorich, Laurent

DOI
10.1016/j.jcsr.2025.109422

Publication date
2025

Document Version
Final published version

Published in
Journal of Constructional Steel Research

Citation (APA)
Xin, H., Li, J., Zhang, Y., Veljkovic, M., Persem, N., & Lorich, L. (2025). Ductile fracture assessment of wire and arc additive manufactured steel materials. *Journal of Constructional Steel Research*, *228*, Article 109422. https://doi.org/10.1016/j.jcsr.2025.109422

Important note
To cite this publication, please use the final published version (if applicable).
Please check the document version above.

Copyright
Other than for strictly personal use, it is not permitted to download, forward or distribute the text or part of it, without the consent of the author(s) and/or copyright holder(s), unless the work is under an open content license such as Creative Commons.

Takedown policy
Please contact us and provide details if you believe this document breaches copyrights.
We will remove access to the work immediately and investigate your claim.

This work is downloaded from Delft University of Technology.
For technical reasons the number of authors shown on this cover page is limited to a maximum of 10.

Green Open Access added to TU Delft Institutional Repository

'You share, we take care!' - Taverne project

https://www.openaccess.nl/en/you-share-we-take-care

Otherwise as indicated in the copyright section: the publisher is the copyright holder of this work and the author uses the Dutch legislation to make this work public.

Journal of Constructional Steel Research 228 (2025) 109422

Contents lists available at ScienceDirect

Journal of Constructional Steel Research

journal homepage: www.elsevier.com/locate/jcsr

Ductile fracture assessment of wire and arc additive manufactured steel materials

Haohui Xin [a,b], Junqiang Li [c], Youyou Zhang [c,*], Milan Veljkovic [d], Nicolas Persem [e], Laurent Lorich [e]

[a] State Key Laboratory of Safety, Durability and Healthy Operation of Long Span Bridges, Southeast University, Nanjing 211189, China
[b] School of Civil Engineering, Southeast University, Nanjing 211189, China
[c] Department of Civil Engineering, School of Human Settlements and Civil Engineering, Xi'an Jiaotong University, Xi'an 710116, China
[d] Civil Engineering and Geosciences, Delft University and Technology, Netherlands
[e] ArcelorMittal Global R&D Bars & Wires, France

ARTICLE INFO

Keywords:
Wire Arc Additive Manufacturing (WAAM)
Ductile fracture simulation
Uncoupled fracture model
Fracture locus
The meso-scale equivalent plastic strain (MSCEPS) methodology

ABSTRACT

This research aims to experimentally investigate the ductile fracture characteristics and the level of anisotropy of four plates, 400 mm × 150 mm × 3.72 mm, made by Wire Arc Additive Manufacturing (WAAM) technology with 1 mm thick layers. Relatively small roughness is measured, expressed in maximum peak-to-valley height, measured by scanning, of 98 μm. Calibrated parameters for an advanced computational material model are derived for a finite element mesh size of 0.5 mm. The experimental campaign is based on eight types of short coupon specimens, analysed to explore fracture behaviour exposed to various stress conditions. Sixty-five coupon specimens, 51 milled and 14 tested in as printed conditions, cut out in three directions relative to the printing direction, are examined. The assumption of isotropic mechanical characteristics is confirmed. The mesoscale critical equivalent plastic strain (MCEPS) methodology is used to predict experimental results numerically. Three stages are considered: elastic, plastic, and couple plastic-damaged stages. The accuracy of the calibrated parameters is validated by comparing the engineering stress-strain relationships obtained from experimental tests and finite element (FE) analysis, reaching very good agreement. A list of all material parameters for ductile fracture modelling at various triaxiality levels and Lode parameters is provided for a mesh size of 0.5 mm.

1. Introduction

Wire and Arc Additive Manufactured (WAAM) technology, harnessing the power of arc welding tools and metal wire, stands out as an efficient process in additive manufacturing. It excels in crafting large-scale components, having the potential to technologically increase deposition rates, further minimise material and equipment expenses, and reach exceptional structural integrity. Ideally suited for the manufacturing of parts of connections or structural members with varying complexity, WAAM presents a compelling alternative to the conventional fabrication processes in civil engineering [1,2]. The exploration of WAAM/GMAW steel applications in the construction sector encompasses a variety of projects, from small scale to the creation of full-scale structures [3–7].

Coupon specimens were cut out to assess the plastic deformation and fracture mechanisms of "GMAW steel plates", facilitating the efficient design of structural components. A comprehensive series of coupon specimen tests were meticulously carried out to thoroughly investigate the mechanical properties of WAAM materials. These properties encompassed key parameters such as the elastic modulus, yield strength, ultimate tensile strength, and fracture strain, providing a holistic assessment of the material's performance. Haden et al. [8] investigated the mechanical properties of WAAM-produced stainless steel 304 and mild steel ER70S. Sun et al. [9] conducted experiments to investigate the anisotropic mechanical properties of a low-carbon, high-strength steel component made by WAAM. Ermakova et al. [10] performed an experimental study on the mechanical and fracture characteristics of WAAM components fabricated from ER70S-6 and ER100S-1 metal wires. Furthermore, the impact of multiple parameters on the mechanical properties has been meticulously examined. This includes the effects of surface roughness, printing orientation, microstructural features, residual stress distribution, and the intricacies of the printing process

* Corresponding author.
E-mail address: youyouzhang@xjtu.edu.cn (Y. Zhang).

https://doi.org/10.1016/j.jcsr.2025.109422
Received 7 February 2025; Accepted 9 February 2025
Available online 18 February 2025
0143-974X/© 2025 Elsevier Ltd. All rights are reserved, including those for text and data mining, AI training, and similar technologies.

Table 1
Specimens used for the tests (Total: 65 specimens).

Specimen	Description	Longitudinal (0^0)	Perpendicular (90^0)	Inclined (45^0)
RR0	As-printed (Raw) dog-bone specimen	5	4	5
MR0	Milled dog-bone specimens	2	3	3
MR3	Milled double round notch specimens with a 3 mm nominal radius	3	3	3
MR6	Milled double round notch specimens with a 6 mm nominal radius	3	3	2
MR12	Milled double round notch specimens with a 12 mm nominal radius	3	1	0
MRV	Milled double sharp notch specimens	3	4	3
MSI	Milled double narrow notch specimens with notch extended to middle line	3	2	3
MSII	Milled double narrow notch specimens with notch extended over middle line	2	1	1

parameters etc. Kyvelou et al. [11] and Laghi [12] conducted extensive tensile tests on WAAM stainless steel, both in as-built and milled conditions, to investigate the printing orientation effects on the mechanical properties. Szost et al. [13] compared the microstructure and residual stress profiles in AM components fabricated by WAAM and the Cladding (CLAD) technique. Wang et al. [14] explored the impact of different arc modes on the tensile properties of 316 L stainless steel specimens manufactured by WAAM. Dinovitzer et al. [15] examined the influence of process parameters on the mechanical properties of WAAM-produced Hastelloy X alloy on 304 stainless-steel substrates. In addition, material models for WAAM steels have also been proposed [16]. These include a quad-linear model and a bilinear plus nonlinear hardening model for normal-strength WAAM steel, as well as a two-stage Ramberg-Osgood model for high-strength WAAM steel. However, to the best of the authors' knowledge, the experimental investigation of ductile fracture in WAAM materials is relatively limited. There is a paucity of research reported on examining the ductile fracture strain in relation to stress triaxiality and the Lode parameters, similar to other metal materials [17].

Finite element analysis (FEA), especially fracture behaviour prediction, is essential for comprehending and enhancing the performance of components manufactured by WAAM, particularly in structural joints. The accuracy of FEA relies on the precise characterisation of material parameters. Identifying material parameters for fracture models is the most important step in the prediction of the failure of steel structures. The phenomenological models [18–20] and physically-based model [21–25] are generally adopted in civil engineering for predicting steel fracture. Uncoupled phenomenological models [26,27] are preferred for their straightforward acquisition of material parameters and simpler computation, in contrast to the more complex physically based models

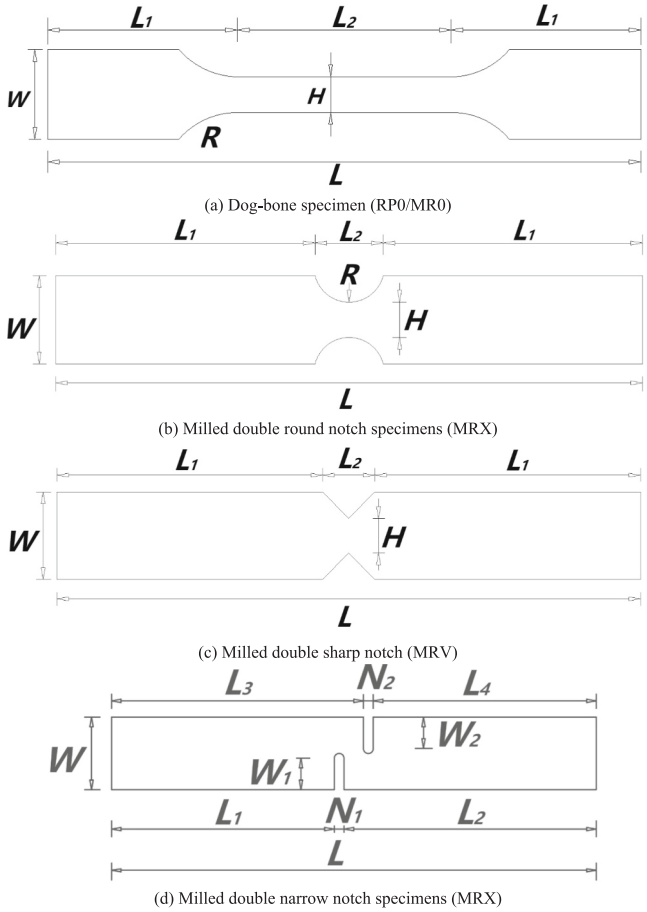

Fig. 1. Geometry and symbols of each specimen.

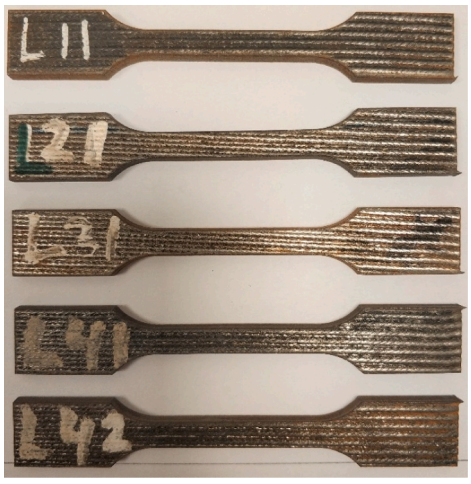

(a) Longitudinal directions (0^0)

(b) Perpendicular directions (90^0)

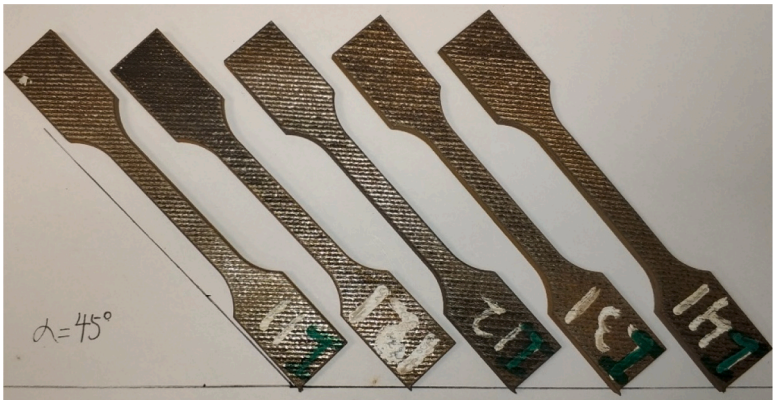

(c) Inclined directions (45^0)

Fig. 2. Photos of as-printed dog-bone specimen.

Fig. 3. Photos of milled 3D printed specimens.

to capture the interaction between deformation and damage processes. The uncoupled phenomenological model assumes that damage progression does not influence the effective stress-strain behaviour of steel. The parameters of the uncoupled phenomenological models are more readily accessible, conducting a series of tailored coupon specimens for each specific component is necessary to accurately identify the parameters essential for the ductile fracture model.

However, while the existing research predominantly concentrates on finite element (FE) predictions of material behaviour prior to necking, to the best of the authors' knowledge, there is a lack of work reported on the ductile fracture predictions for WAAM steels. Therefore, the experimental results from 65 coupon specimens made from a Wire Arc Additive Manufacturing (WAAM) plate using the Gas Metal Arc Welding (GMAW) process are used to determine fracture properties. Out of the 65 specimens, 51 were milled to a uniform finish, and 14 were tested with the surface as it was when printed. Eight distinct types of relatively short specimens, with basic dimensions according to ASTM E8/E8M-13 [28], are analysed to explore fracture behaviour under various stress conditions. In the material model, we considered three critical regions of the stress-strain curve derived from uniaxial testing: the elastic stage, which

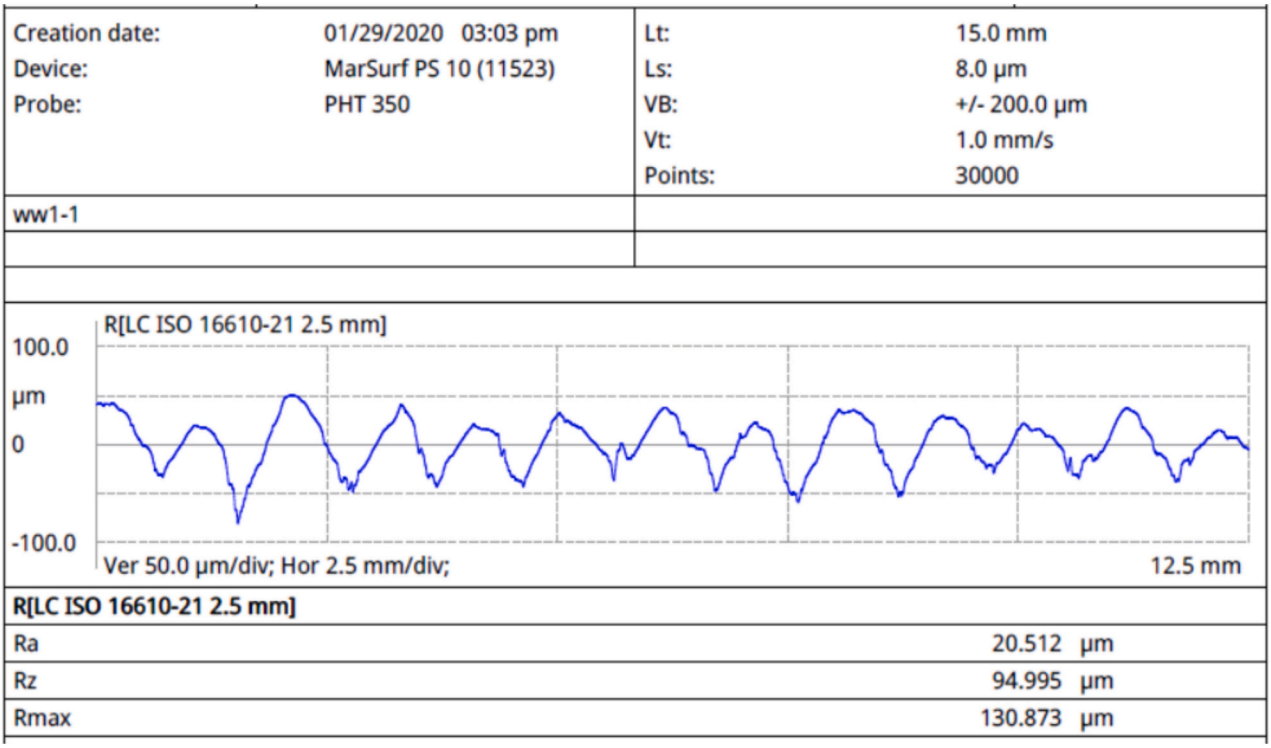

Fig. 4. Illustration of surface roughness measurements for 3D printed materials.

Table 2
Results of roughness measurement of 3D printed plates with directions of 90^0 (Unit: µm).

Specimen		R_z				R_{max}			
		1st	2nd	3rd	Ave	1st	2nd	3rd	Ave
Plate 1	Side A	95.0	84.4	91.8	90.40	130.9	104.2	101.3	112.13
	Side B	89.6	101.1	85.6	92.10	104.8	126.6	110.4	113.93
Plate 2	Side A	85.9	87.6	97.3	90.27	90.7	101.1	110.9	100.90
	Side B	95.6	90.4	79.5	88.50	111.7	99.2	85.5	98.80
Plate 3	Side A	81.8	76.3	53.2	70.43	102.7	90.7	65.4	86.27
	Side B	64.3	60.0	53.3	59.20	80.7	65.4	65.4	70.50
Plate 4	Side A	88.9	95.9	86.4	90.40	111.1	111.7	108.5	110.43
	Side B	98.8	86.1	77.3	87.40	106.5	93.2	84.5	94.73
		Average			83.59	Average			98.46

Table 3
Results of roughness measurement milled of 3D printed plates with directions of 45^0 and 0^0 (Unit: µm).

Specimen		R_z				R_{max}			
		1st	2nd	3rd	Ave	1st	2nd	3rd	Ave
Plate 1	45^0	14.0	12.4	13.1	13.17	23.5	15.6	20.3	19.80
Plate 1	0^0	5.6	4.7	6.7	5.67	6.6	5.5	8.2	6.77

marks the initial linear response of the material; the plastic stage, where permanent deformation sets in beyond the material's yield point; and the coupled plastic-damage stage, reflecting the complex interaction between plastic flow and material degradation. The ductile fracture behaviour of WAAM steel is predicted by the meso-scale equivalent plastic strain (MSCEPS) approach proposed by the authors [29,30]. To prove the accuracy of the calibrated parameters, the experimentally derived engineering stress-strain relationship is compared with the predictions generated by finite element (FE) analysis. Such comparative assessment ensures the validation of the model's predictive capabilities.

2. Experimental details and results

2.1. Coupon specimens

Four plates were manufactured using Gas Metal Arc Welding (GMAW) technology, as a subset of Wire Arc Additive Manufacturing (WAAM). The specific type of welding wire, its chemical composition, and the mechanical properties used in the GMAW process were provided in the authors' previous publication [7].

A comprehensive test series was conducted on eight distinct types of specimens to explore the fracture behaviour under various stress conditions. Specimens' details per category are given in Table 1. Additionally, the layout and corresponding symbols for each specimen are

Table 4
Experimental results summary of as-printed dog-bone (RR0) specimens and nominal values of the electrode.

Direction	Label	Thickness (mm)	Width (mm)	Elastic modulus (GPa)	Yield strength (MPa)	Ultimate strength (MPa)	Uniform elongation (%)
	RR0L1	3.74	4.89	199.7	401.0	544.0	31.0
	RR0L2	3.63	4.87	209.8	406.0	551.0	27.0
0^0	RR0L3	3.64	4.87	203.3	425.0	550.0	32.0
	RR0L4	3.74	4.88	214.3	412.0	551.0	34.0
	RR0L5	3.76	4.87	188.2	385.0	546.0	32.0
Average				197.6	404.0	548.0	29.0
	RR0I1	3.63	4.88	188.4	411.0	545.0	32.0
	RR0I2	3.67	4.88	206.8	407.0	544.0	33.0
45^0	RR0I3	3.69	4.88	191.3	417.0	547.0	31.0
	RR0I4	3.68	4.88	192.5	420.0	548.0	31.0
	RR0I5	3.64	4.88	193.8	391.0	550.0	32.0
Average				204.8	409.0	544.0	32.0
	RR0P1	3.82	4.88	191.1	350.0	534.0	30.0
90^0	RR0P2	3.83	4.89	196.5	403.0	564.0	31.0
	RR0P3	3.85	4.88	193.3	357.0	542.0	31.0
	RR0P4	3.76	4.88	196.1	349.0	537.0	31.0
Average				194.2	365.0	544.0	31.0
ER70S-6 wire based on EN ISO 636 [31]					480.0	580.0	24.0

Table 5
Experimental results summary of milled dog-bone (MR0) specimens.

Direction	Label	Width (mm)	Thickness (mm)	Elastic modulus (GPa)	Yield strength (MPa)	Ultimate strength (MPa)	Uniform elongation (%)
0^0	MR0L1	6.17	2.82	210.8	401.6	575.6	27.4
	MR0L2	6.00	2.81	204.2	382.8	564.0	30.0
Average				207.5	392.2	569.8	28.7
	MR0I1	5.88	2.82	182.2	428.9	570.2	32.0
45^0	MR0I2	6.00	2.81	206.9	418.4	576.8	32.5
	MR0I3	6.00	2.81	185.4	393.8	575.4	31.2
Average				191.5	413.7	574.1	31.9
	MR0P1	6.11	2.87	216.7	455.7	598.2	31.0
90^0	MR0P2	6.00	2.81	199.4	408.7	577.3	32.1
	MR0P3	6.05	2.87	182.8	394.0	573.6	34.5
Average				199.6	419.5	583.0	32.5
ER70S-6 wire based on EN ISO 636 [31]					480.0	580.0	24.0

shown in Fig. 1.

Specimens were cut out from four plates, oriented at 0° (direction parallel to the main printing layer), 45° (inclined), and 90° (perpendicular to the main printing layer), to assess the material's anisotropic properties systematically. Typical specimens, as-printed and oriented at 0°, 45°, and 90° for cutting, are illustrated in Fig. 2. Fig. 3 shows photographs of the MR0, MR3, MR6, MR12, MSI, and MSII specimens, arranged from left to right. The MR0 specimens are subjected to uniaxial tension, while the MR3, MR6, MR12, and MRV specimens have equibiaxial tension in the critical section. Additionally, the MSI and MSII specimens are exposed to a combination of tension and shear stress [29,30]. Consequently, the specimen nomenclature in the subsequent sections should explicitly incorporate the cutting direction, angle, specimen type, and identifier. The specimen designations adhere to a standardised format, specified as 'specimen type - direction - specimen number within the same batch'. The classification of specimen types is delineated in Table 1. Noted that "L" denotes cutting longitudinal to the direction of the printing (0° direction), "P" denoted that cutting perpendicular to the direction of the printing (90° direction), and "I" denoted that cutting inclined to the direction of the plate (45° direction). For example, the specimen designated as MR3L1 represents the first milled specimen featuring a double round notch with a nominal radius of 3 mm, which has been cut along the direction of the printing, corresponding to the 0° orientation.

2.2. Roughness measurements

The surface roughness of the 3D printed plates was measured using a Marsurf PS10 profilometer. A total of three measurements were taken at distinct positions on each of the four plates, ensuring a comprehensive assessment of the surface characteristics. Fig. 4 illustrates an example of surface roughness measurements. The mean peak-to-valley height is represented by the parameter R_z, while the maximum peak-to-valley height is indicated by R_{max}. The surface roughness measurements of both sides of the plates are given in Tables 2 and 3.

For the 3D printed plates oriented in the 90^0 direction, as shown in Table 2, the average Rz is 83.59 μm, and the average R_{max} is 98.46 μm. The maximum R_z value recorded is 101.1 μm, with the minimum at 53.2 μm, while the maximum R_{max} value is 130.9 μm and the minimum is 65.4 μm. The average Rz value for plate 1, oriented at a 45-degree angle, is 13.17 μm, with the corresponding average Rmax value being 19.80 μm. When direction of measurements is oriented 0-degree angle, plate 1 exhibits a lower average Rz value of 5.7 μm and an average Rmax value of 6.8 μm.

2.3. Test results of dog-bone specimens

The geometrical dimensions, i.e. the width (H) and thickness (t), as well as the experimental test outcomes, showing the elastic modulus,

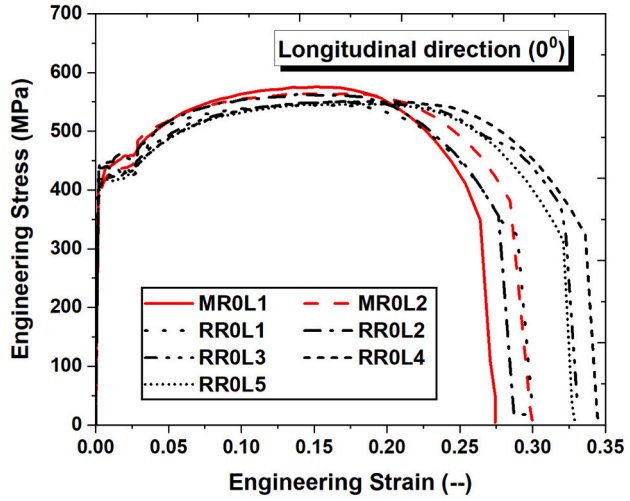

(a) Longitudinal direction (0^0)

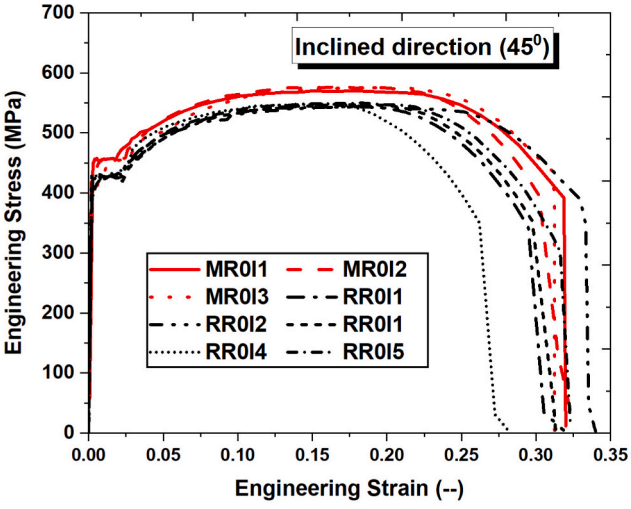

(b) Inclined direction (45^0)

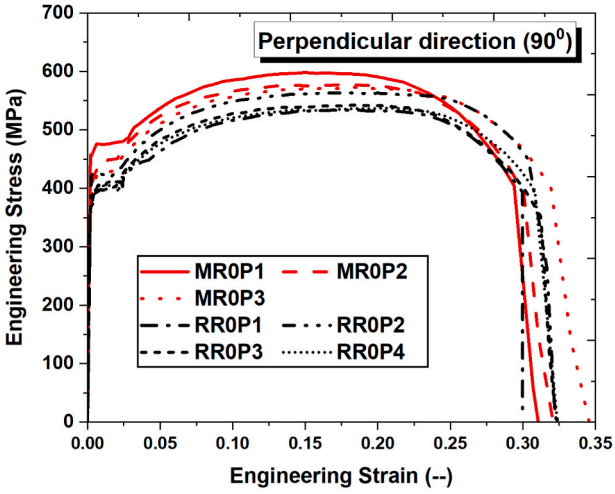

(c) Perpendicular direction (90^0)

Fig. 5. Engineering stress-strain relationship of dog-bone specimens.

Table 6
Printing direction effects on the mechanical performance of dog-bone specimens.

Type	Variation	Elastic modulus (GPa)	Yield strength (MPa)	Ultimate strength (MPa)	Uniform elongation (%)
As-printed	$R = \frac{X_{45}}{X_0} - 1.0$	3.64 %	1.24 %	−0.73 %	10.34 %
	$R = \frac{X_{90}}{X_0} - 1.0$	−1.72 %	−9.65 %	−0.73 %	6.90 %
Milled	$R = \frac{X_{45}}{X_0} - 1.0$	−7.71 %	5.48 %	0.75 %	11.15 %
	$R = \frac{X_{90}}{X_0} - 1.0$	−3.81 %	6.96 %	2.32 %	13.24 %

Table 7
Surface roughness effects on the mechanical performance of dog-bone specimens.

Type	Degree	Elastic modulus (GPa)	Yield strength (MPa)	Ultimate strength (MPa)	Uniform elongation (%)
$R = \frac{X_{milled}}{X_{as-printed}} - 1.0$	0^0	5.01 %	−2.92 %	3.98 %	−1.03 %
	45^0	−6.49 %	1.15 %	5.53 %	−0.31 %
	90^0	2.78 %	14.93 %	7.17 %	4.84 %

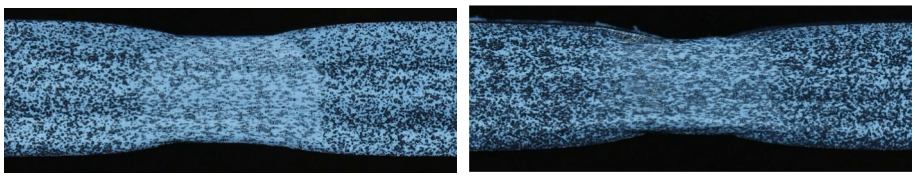

(a) RR0L1 (0^0 Directions)

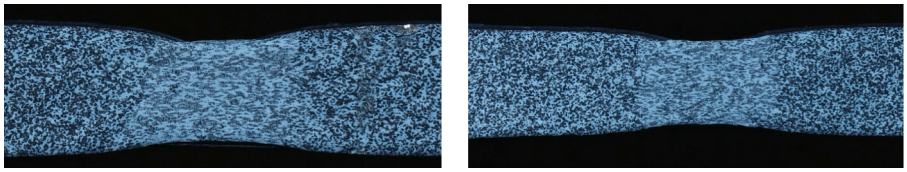

(b) RR0I2 (45^0 Directions)

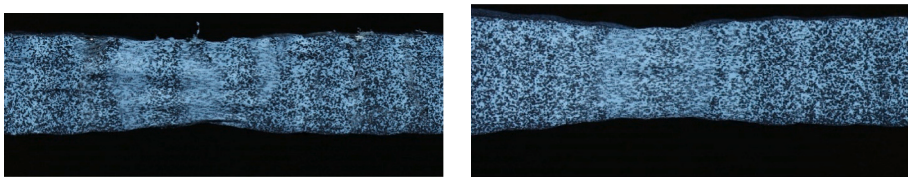

(c) RR0P3 (90^0 Directions)

Fig. 6. Failure mode of as-printed dog-bone (RR0) specimens.

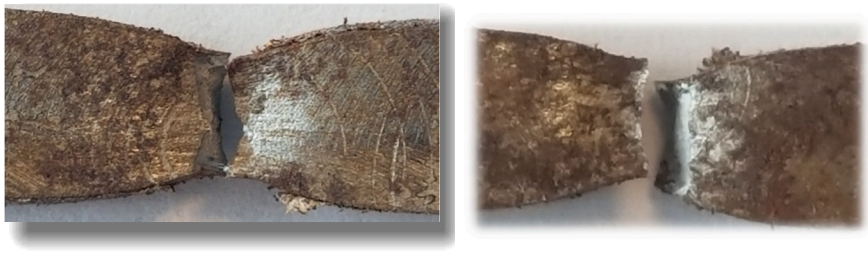

(a) MR0L1 (0^0 Directions)

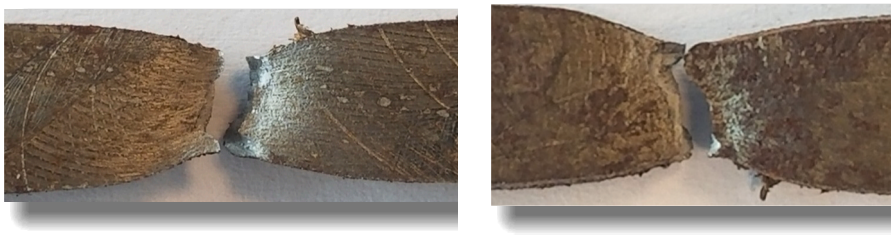

(b) MR0I2 (45^0 Directions)

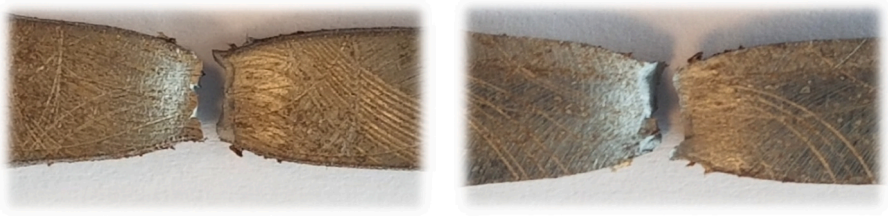

(c) MR0P1 (90^0 Directions)

Fig. 7. Failure mode of milled dog-bone (MR0) specimens.

Table 8
Experimental results of milled double round notch specimens.

Directions	Label	W	L	H	R	t	Yield strength (MPa)	Ultimate strength (MPa)	Uniform elongation (%)
		mm	mm	mm	mm	mm			
0^0	MR3L1	14.9	99.8	6.2	3.0	2.82	460.85	636.14	36.54
	MR3L2	15.0	100.1	5.9	3.0	2.85	449.83	660.39	38.47
	MR3L3	14.0	98.9	5.4	3.0	2.84	483.98	607.04	31.80
	Average						464.89	634.52	35.60
	MR6L1	15.3	100.0	6.2	6.0	2.82	464.57	620.17	25.03
	MR6L2	14.9	100.0	6.1	6.0	2.83	453.12	607.20	23.80
	MR6L3	15.0	100.0	6.0	6.0	2.85	470.68	608.64	23.78
	Average						462.79	612.00	24.20
	RP12L1	15.2	99.9	6.1	12.0	2.82	436.36	609.64	17.60
	RP12L2	15.3	99.7	6.3	12.0	2.85	408.54	588.61	17.49
	RP12L3	15.0	100.0	5.9	12.0	2.82	418.64	597.06	17.45
	Average						421.18	598.44	17.51
45^0	MR3I1	14.1	99.1	5.1	3.0	2.73	479.71	638.07	37.34
	MR3I2	14.9	100.0	5.9	3.0	2.81	455.13	663.91	39.87
	MR3I3	10.0	100.2	4.2	3.0	2.82	478.10	617.75	33.82
	Average						470.98	639.91	37.01
	MR6I1	14.1	99.1	5.1	6.0	2.73	428.67	583.06	23.79
	MR6I2	12.0	98.8	5.1	6.0	2.82	488.12	624.48	22.10
	Average						458.40	603.77	22.95
90^0	MR3P1	15.0	99.9	6.2	3.0	2.90	472.19	665.82	36.51
	MR3P2	14.7	100.1	5.9	3.0	2.85	457.78	646.45	37.03
	MR3P3	10.0	100.0	4.0	3.0	2.82	414.26	628.97	33.75
	Average						448.08	647.08	35.76
	MR6P1	15.1	99.9	6.2	6.0	2.89	441.56	619.76	23.81
	MR6P2	13.0	100.0	5.0	6.0	2.82	489.69	629.10	22.09
	MR6P3	15.0	100.0	6.0	6.0	2.87	478.86	629.23	25.05
	Average						470.04	626.03	23.65
	RP12P1	15.0	100.0	6.0	12.0	2.92	410.06	604.71	17.95

yield strength, ultimate tensile strength, and uniform elongation, for both as-printed (RR0) and milled (MR0) dog-bone specimens are given in Tables 4 and 5, respectively. The mechanical properties of steel wires used during 3D printing are also listed based on EN ISO 636 A [31]. The recommended values of ISO standards are characteristic values representing the lower fractal of the mechanical property. The definitions of the symbols are provided in Fig. 1. The engineering stress-strain relationships for dog-bone specimens are depicted in Fig. 5. Note that the engineering strain is determined by calculating the average ratio of the incremental displacement to the original gauge length, which is 25 mm, with the smallest area of interest being the necking region in the middle. A summary of the material characteristics affected by the printing direction and surface roughness is listed in Table 6 and 7. In reviewing the impact of surface roughness on material properties, the discrepancies in elastic modulus are observed within a range of 3 % to 7 %. Yield strength displays a more pronounced variation, ranging from 1 % to 15 %, whereas the ultimate strength exhibits a moderate deviation, with differences between 4 % and 7 %. Uniform elongation is relatively unaffected, with 0 % to 5 % variations. Regarding the influence of printing direction, variations in the elastic modulus are noted within a narrow margin of 2 % to 8 %. The yield strength exhibits a larger fluctuation, spanning from 1 % to 10 %. In contrast, the ultimate strength shows a moderate deviation, with discrepancies falling between 0 % and 2 %. The uniform elongation remains largely invariant, with variations confined to a range of 7 % to 13 %. Except for the yield strength in the direction perpendicular to the printing axis, the variations are considered negligible, as they belong to the inherent variability within the same production batch.

The failure mode of the as-printed dog-bone (RR0) specimens is shown in Fig. 6, while the corresponding failure characteristics for the milled dog-bone (MR0) specimens are given in Fig. 7. Significant necking is evident in both as-printed and milled specimens across all three orientations before the final fracture. The failure mode of milled specimens exhibits similarity for different orientations, suggesting that directional effects on failure mode are minimal. In contrast, the failure modes in as-printed specimens depend on various orientations.

2.4. Test results of milled double round notch specimens

Table 8 shows the geometrical dimensions of the milled double round notch specimens (MRx), including total width (W), width at the double round notch (H), total length (L), nominal radius of the round notch (R), and thickness (t). The above symbols are presented in Fig. 1. The experimental results of the milled double round notch specimens are shown in Fig. 8. Note that Engineering strain is calculated as the average ratio of the incremental displacement to the original gauge length, depending of the diameters of the round notches. Table 9 is a summary showing how the printing directions influence the material characteristics of MRx specimens. Influenced by the printing direction, the yield strength demonstrates significant variability, ranging from 1 % to 4 %. The ultimate strength exhibits a more moderate divergence, with discrepancies ranging between 1 % and 2 %. Uniform elongation, however, remains predominantly constant, with fluctuations limited to a narrow band of 0 % to 5 %. These variations are considered to be within the typical scatter observed in standard material testing procedures.

Figs. 9, 10, and 11 show the failure modes for the MR3, MR6, and MR12 specimens. These illustrations emphasise how the printing direction influences the failure mode. It is observed that all specimens

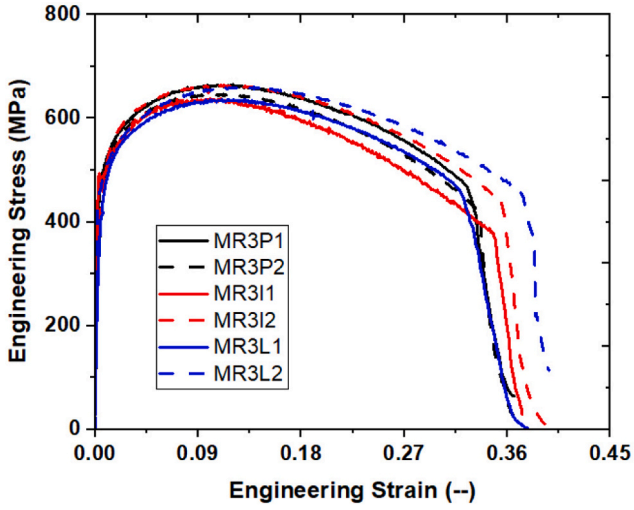

(a) MR3 specimens (W=15mm)

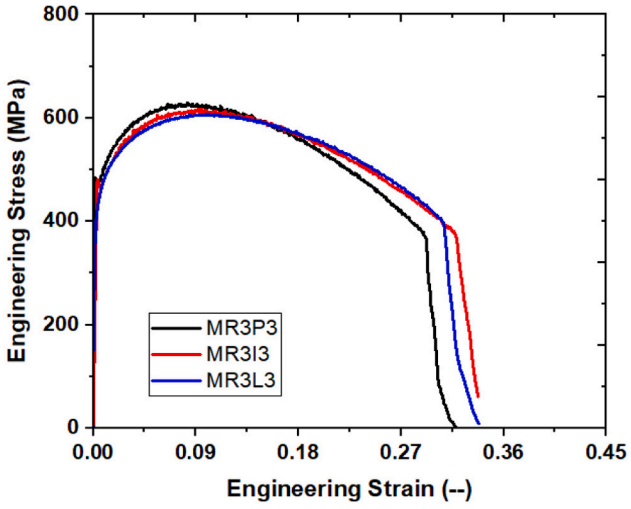

(b) MR3 specimens (W=10mm)

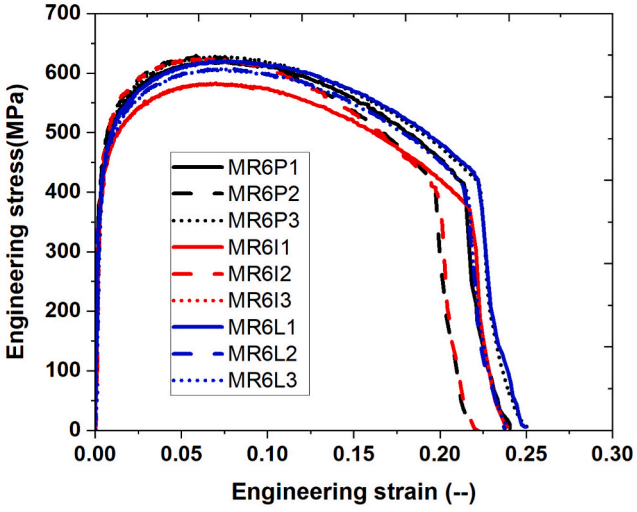

(c) MR6 specimens

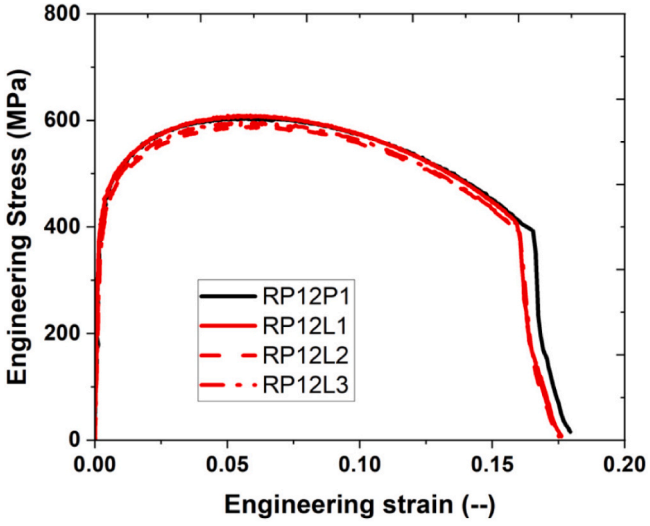

(d) MR12 specimens

Fig. 8. Engineering stress-strain relationship of double notched specimens.

Table 9
Printing direction effects on the mechanical performance of milled double notch specimens.

Type	Variation	Yield strength (MPa)	Ultimate strength (MPa)	Uniform elongation (%)
MR3	$R = \frac{X_{45}}{X_0} - 1.0$	1.31 %	0.85 %	3.96 %
	$R = \frac{X_{90}}{X_0} - 1.0$	−3.62 %	1.98 %	0.45 %
MR6	$R = \frac{X_{45}}{X_0} - 1.0$	−0.95 %	−1.34 %	−5.17 %
	$R = \frac{X_{90}}{X_0} - 1.0$	1.57 %	2.29 %	−2.27 %
MR12	$R = \frac{X_{45}}{X_0} - 1.0$	–	–	–
	$R = \frac{X_{90}}{X_0} - 1.0$	−2.64 %	1.05 %	2.51 %
MRV	$R = \frac{X_{45}}{X_0} - 1.0$	3.19 %	1.26 %	−14.12 %
	$R = \frac{X_{90}}{X_0} - 1.0$	3.05 %	5.49 %	2.27 %

experience failure at their smallest cross-sectional areas. The fracture patterns, in all cases, is along "the shortest line" perpendicular to the axis of the specimens. The MR3 specimens do not have necking in any of the directions tested. While the MR6 specimens display a minor necking around the cross-section of the fracture for all directions. For the MR12 specimens, there is a clear difference in failure characteristics based on the direction. In the 0^0 direction, necking is evident, indicating a ductile failure mode. On the contrary, the 90^0 direction specimens show a "flat fracture" surface, indicating an abrupt fracture.

2.5. Test results of milled double "V" notch specimens

Table 10 gives the dimensions of the milled double "V" notch specimens (MRV), with the total width (W), width at the double "V" notch (H), total length (L), and thickness (t). The definitions of the aforementioned symbols are also shown in Fig. 1. Additionally, the table includes experimental results, namely yield strength, ultimate tensile strength, and uniform elongation. The engineering stress-strain relationships for the double sharp notch specimens are shown in Fig. 12. Note that the engineering strain is determined by calculating the average ratio of the incremental displacement to the distance of the sharp notch symmetrically on each side of the notch. A summary that accounting on the influence of printing directions and the material characteristics of MRV specimens is listed in Table 9. The printing direction exerts a minor influence on the yield strength, with variations amounting to approximately 3 %. The ultimate strength exhibits discrepancies within a range of 1 % to 6 %. Notwithstanding these fluctuations, uniform elongation remains relatively stable, with variations confined to a band of 2 % to 12 %. These observed variations are within the typical scatter expected in standard material testing procedures.

Fig. 13 shows the failure modes of MRV specimens, highlighting the influence of different printing directions on fracture surface. Each specimen fracture at the minimal cross-section area. Along the 0^0 and 90^0 directions, MRV specimens show a modest level of necking, indicating a short phase of ductility before the fracture. On contrary, when aligned in the 45^0 directions, these specimens do not have necking, indicating a brittle fracture.

2.6. Test results of milled double narrow notch specimens

Table 11 provides an overview of the dimensions for milled double narrow notch specimens (MSx), with total width (W), total length (L), the lengths up to the narrow notches on either side (L1 and L2), notch lengths (W1 and W2), notch widths (N1 and N2), and thickness (t). Check the symbols shown in Fig. 1. Fig. 14 shows the engineering stress-strain relationships of the double narrow notch specimens. The engineering strain is defined by the mean ratio of the change in displacement to the initial gap width, referring to the dimensions of the narrow notches along the specimen's edge. A summary is depicted in Table 12 considers the possible influence of the printing direction on the material characteristics on MSx specimens. The MSI specimens exhibit a comparatively minor variation in terms of yield strength, ultimate strength, and uniform elongation, as opposed to the MSII specimens.

The failure modes of milled double narrow notch (MS) specimens are shown in Fig. 15. A 45^0-degree inclined fracture surface is observed for both MSI and MSII specimens indicating the failure mechanism characterised by shear loading. Although the MSI and MSII specimens both exhibit fractures inclined at 45^0 degrees, the positions of crack origination are distinct: MSI specimens are prone to midsection cracking, while MSII specimens are more likely to fracture close the outer edges. The deformation in the slender plates between the notches is considerably more pronounced in MSII specimens, indicating the ductile behaviour and enhancing capacity for plastic deformation compared to MSI specimens. The distinct fracture patterns shows that the MSI specimens exhibit cracks that form a characteristic inclined surface, suggesting a less ductile failure mode compared to MSII specimens where the local necking is visible. Noted that the uniform elongation has no physical meaning for the tensile-shear dominated specimens, just for the sake of comparing between FE and tests considering geometry scatter during fabrication.

3. Ductile fracture simulation

3.1. Calibration of materials parameters

The fundamental assumption of the uncoupled ductile fracture material model assumes that the progression of damage does not influence

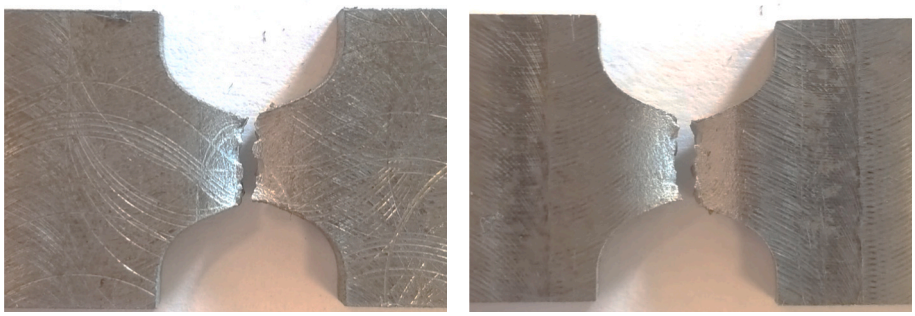

(a)MR3L2 (0^0 Directions)

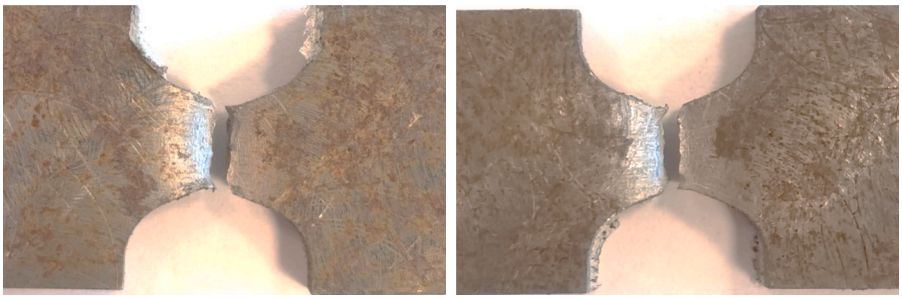

(b) MR3I3 (45^0 Directions)

(c)MR3P1 (90^0 Directions)

Fig. 9. Failure mode of MR3 specimens.

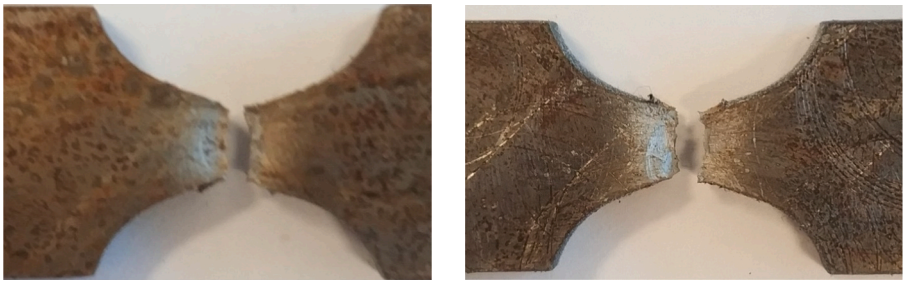

(a) MR6L2 (0^0 Directions)

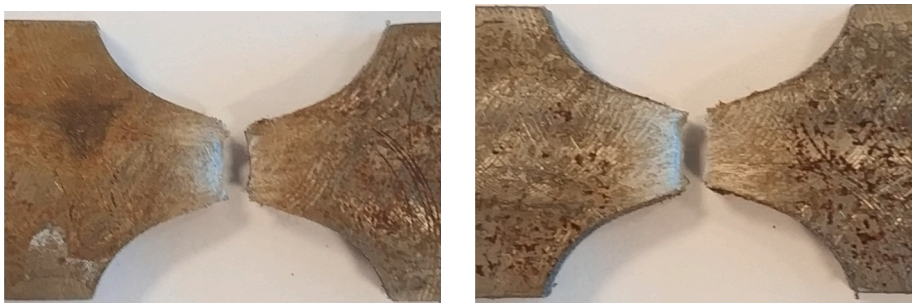

(b) MR6I3 (45^0 Directions)

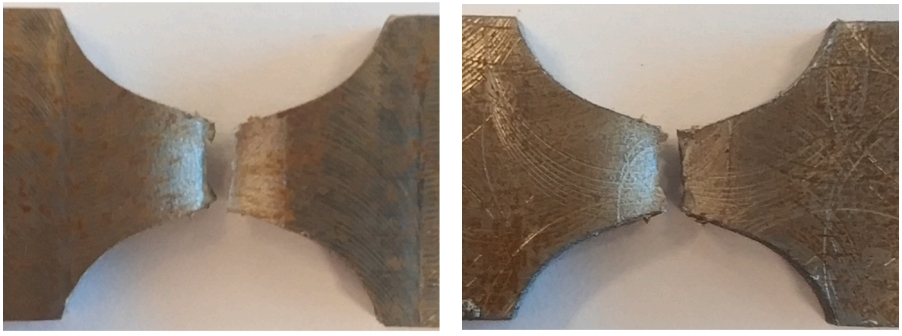

(c) MR6P1 (90^0 Directions)

Fig. 10. Failure mode of MR6 specimens.

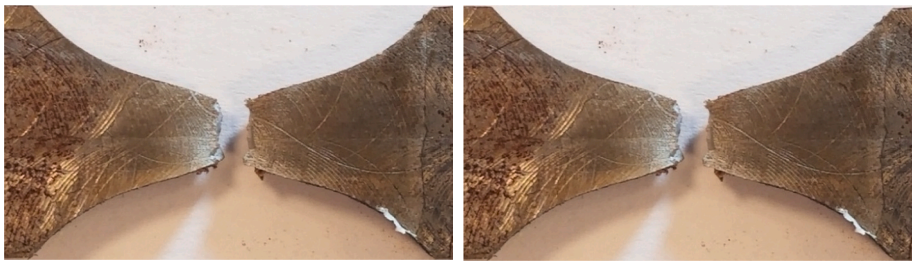

(a) RP12L3 (0^0 Directions)

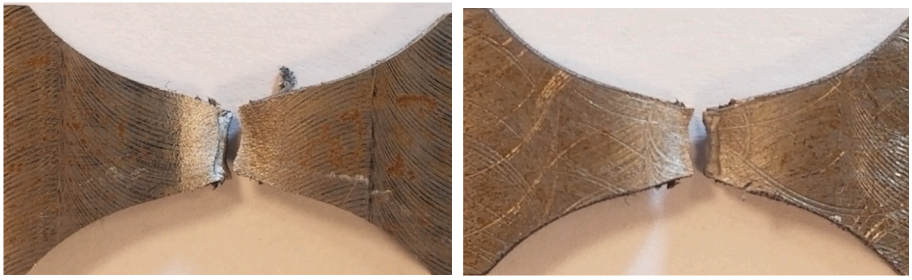

(b) RP12P1 (90^0 Directions)

Fig. 11. Failure mode of MR12 specimens.

Table 10
Experimental results of milled double sharp notch (MRV) specimens.

Directions	Label	W	L	H	t	Yield strength (MPa)	Ultimate strength (MPa)	Uniform elongation (%)
		mm	mm	mm	mm			
0^0	MRVL1	14.6	99.8	6.6	2.85	448.89	615.23	26.88
	MRVL2	15.0	100.0	6.2	2.82	461.34	677.84	29.20
	MRVL3	14.1	98.9	5.5	2.84	470.78	620.87	20.43
	Average					460.34	637.98	25.50
45^0	MRVI1	14.2	99.1	5.5	2.71	455.77	628.20	22.47
	MRVI2	14.9	99.9	6.6	2.80	480.62	650.89	22.77
	MRVI3	15.2	99.8	6.4	2.86	488.71	659.00	20.46
	Average					475.03	646.03	21.90
90^0	MRVP1	14.9	100.0	6.0	2.84	491.28	696.45	27.82
	MRVP2	15.0	100.0	6.0	2.84	461.85	685.60	24.33
	MRVP3	15.1	100.0	6.2	2.88	465.08	666.06	26.32
	MRVP4	14.6	100.0	6.4	2.89	479.25	643.97	25.86
	Average					474.37	673.02	26.08

the true stress-strain relationship of 3D printed steel until the point of fracture. This section systematically calibrates the relationship between uniaxial true stress and equivalent plastic strain, as well as the parameters defining the fracture locus.

3.1.1. *Plastic flow stress*

Milled dog-bone like specimens were used as a calibration base for the plastic flow stress of 3D-printed steel. The detailed dimensions these specimens are shown in Fig. 1 and Table 5. The variability of obtained results in the mechanical behaviour identifying the upper and lower envelopes, as well as the average line, are shown in Fig. 16. Nominal values of used electrodes are given for the sake of comparison. Statistical assessment of variations is left out of the scope of this work.

When subjected to uniaxial loading three key phases are distinguished: the initial elastic stage (From 0.0 to Point B in Fig.16), followed by the plastic stage (From Point A to Point B in Fig.16), and the plastic-damage coupled stage (From Point B to Point C in Fig.16). This sequential transformation delineates the mechanical response of the material under tensile loading [32]. During the elastic stage, the behaviour of the material is governed by the elastic strain $\varepsilon^e$and the modulus of elasticity E. This stage is defined by the material's ability to return to its original shape upon the removal of the applied load, according to Hooke's Law, which states that stress is linearly dependent on strain. In the plastic stage, the true stress-strain relationship is determined from the engineering stress-strain data extracted from the milled dog-bone specimens. This conversion is essential for an accurate representation of the material's behaviour beyond its elastic limit, as given by Eqs. (1) and (2).

$$\sigma_t = \sigma_e(1+\varepsilon_e) \tag{1}$$

$$\varepsilon_t = ln(1+\varepsilon_e) \tag{2}$$

where: σ_t and ε_t are the true stress and true strain; σ_e and ε_e are the engineering stress and engineering strain.

Eqs. (1) and (2) are crucial for understanding the initial stages of plastic deformation. Still, they do not account for the complexities introduced by necking and material damage that occur as deformation increases. Therefore, there is a need for a more sophisticated model that encompasses these phenomena to maintain applicability throughout the entire deformation process. The plastic-damage coupled stage distinguishes two specific sub-phases: the plastic-dominated phase and the damage-dominated phase. This refinement emphasised the evolving

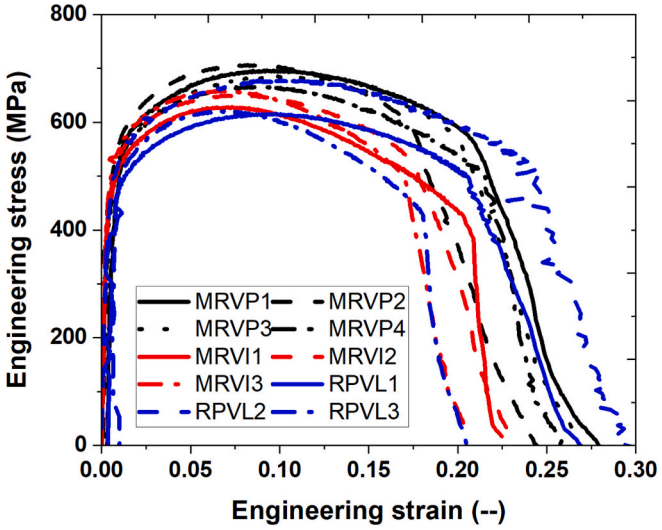

Fig. 12. Engineering stress-strain relationship of milled double sharp notch specimens.

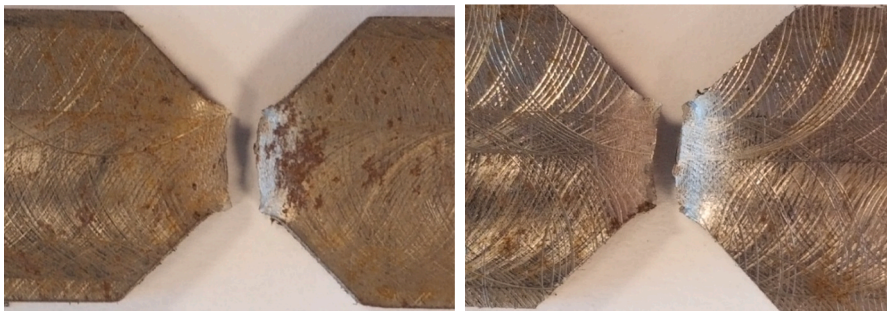

(a) MRVL2 (0^0 Directions)

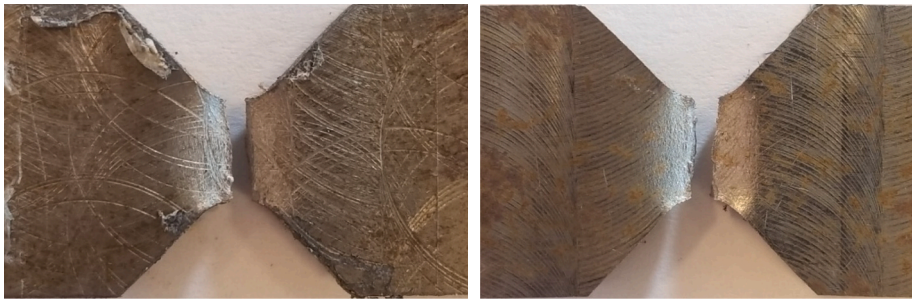

(b) MRVI2 (45^0 Directions)

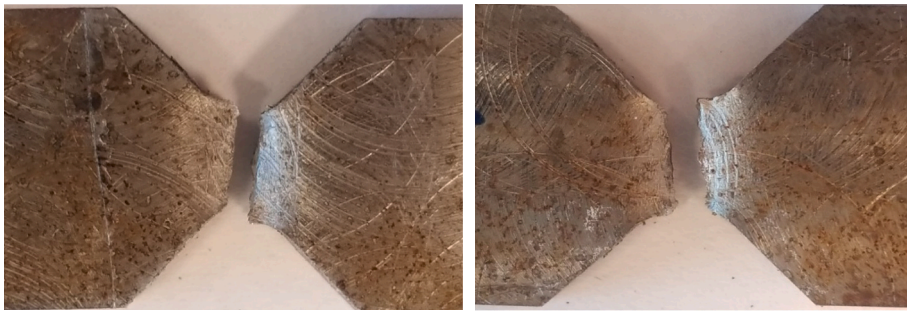

(c) MRVP1 (90^0 Directions)

Fig. 13. Failure mode of milled double sharp notch specimens.

Table 11
Experimental results of milled double narrow notch specimens.

Directions	Label	W mm	L mm	L_1 mm	L_3 mm	W_1 mm	W_2 mm	N_1 mm	N_2 mm	t mm	Yield strength (MPa)	Ultimate strength (MPa)	Uniform elongation (%)
	MSIL1	14.9	100.0	51.9	45.9	7.6	7.3	2.1	2.3	2.84	159.01	300.01	258.35
	MSIL2	15.0	99.8	52.5	46.1	7.4	7.3	2.2	2.0	2.83	146.39	330.96	302.46
	MSIL3	14.2	99.0	51.0	44.9	7.1	7.2	3.1	3.1	2.83	144.69	249.83	246.86
0^0	Average										150.03	293.6	269.22
	MSIL1	15.0	100.0	52.0	46.0	9.4	9.6	2.0	2.1	2.80	123.	284.10	403.60
	MSIL2	15.0	99.6	51.6	45.4	9.4	9.3	2.4	2.4	2.85	122.27	266.57	403.03
	Average										122.64	275.33	403.32
	MSII1	14.9	100.0	52.1	45.9	7.5	7.5	2.0	2.2	2.82	150.10	285.35	218.46
45^0	MSII2	14.9	100.0	51.9	45.9	7.5	7.5	2.2	2.2	2.81	152.67	285.13	226.36
	Average										151.39	285.24	222.41
	MSIII1	14.0	99.2	51.1	45.2	7.5	7.6	3.1	2.9	2.72	130.09	288.50	514.64
	MSIP1	15.0	100.0	51.9	46.0	7.5	7.3	2.1	2.1	2.90	145.86	272.57	254.65
	MSIP2	14.9	100.0	52.0	45.9	7.5	7.4	2.1	2.2	2.87	141.08	298.13	270.73
90^0	MSIP3	15.0	100.0	52.2	45.9	7.6	7.6	1.9	2.1	2.89	131.15	271.28	245.59
	Average										139.36	280.66	256.99
	MSIIP1	14.7	100.0	52.0	46.0	8.2	8.2	2.1	2.0	2.89	105.43	278.03	509.90

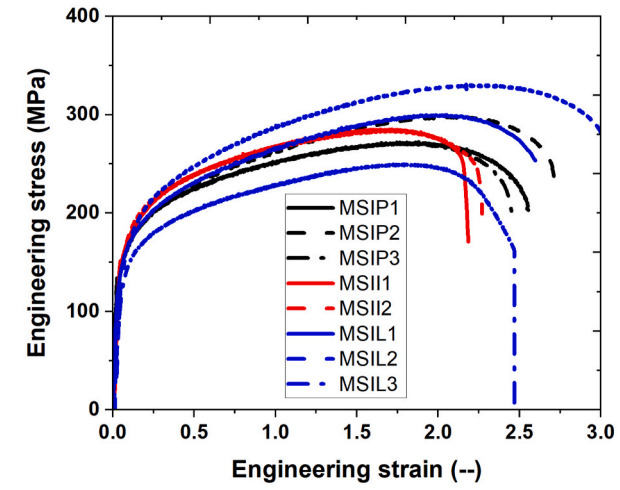

(a) MSI specimens

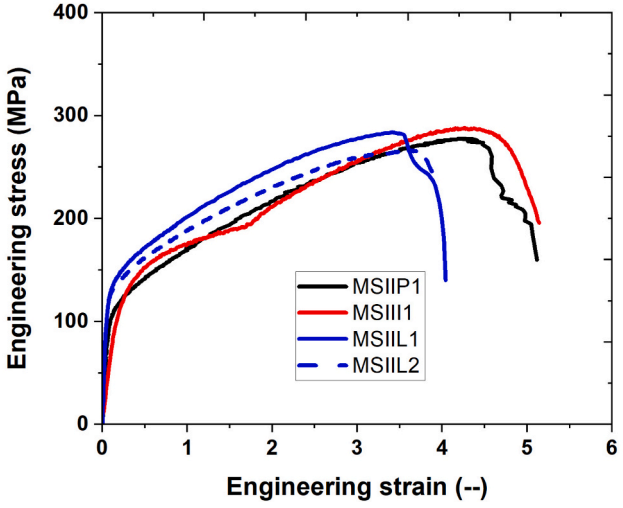

(b) MSII specimens

Fig. 14. Engineering stress-strain relationship of milled double narrow notch specimens.

Table 12
Printing direction effects on the mechanical performance of milled double notch specimens.

Type	Variation	Yield strength (MPa)	Ultimate strength (MPa)	Uniform elongation (%)
MSI	$R = \frac{X_{45}}{X_0} - 1.0$	0.91 %	−2.85 %	−17.39 %
	$R = \frac{X_{90}}{X_0} - 1.0$	−7.11 %	−4.41 %	−4.54 %
MSII	$R = \frac{X_{45}}{X_0} - 1.0$	6.07 %	4.78 %	27.60 %
	$R = \frac{X_{90}}{X_0} - 1.0$	−14.03 %	0.98 %	26.43 %

interplay between plastic deformation and material damage, allowing for a more nuanced and accurate depiction of the material's behaviour exposed to high deformations (strains). In the plastic-dominated stage, the relationship in Eq. (3) between true stress and true strain is articulated through the weighted average model, as referenced in [33].

$$\overline{\sigma}^{neck} = \overline{\sigma}_u \left[W\left(1 + \overline{\varepsilon}^p - \overline{\varepsilon}_u^p\right) + (1 - W)\left(\frac{(\overline{\varepsilon}^p)^{\overline{\varepsilon}_u^p}}{(\overline{\varepsilon}_u^p)^{\overline{\varepsilon}_u^p}}\right) \right] \tag{3}$$

where: W represents a weight constant and $0 \leq W \leq 1$; $\overline{\varepsilon}_u^p$ and $\overline{\sigma}_u$ are the corresponding plastic strain and true stress at the end of plastic phase; $\overline{\varepsilon}^p$ and $\overline{\sigma}^{neck}$ are plastic strain and true stress after necking, respectively.

In the plastic-damage coupled stage, particularly when damage is the predominant factor, the relationship between true stress and plastic strain [32] is articulated through Eq. (4).

$$\overline{\sigma} = \left[\sum_{i}^{n} (1 - d_i) \right] \overline{\sigma}^{neck} \ (i = 1 \ldots . n) \tag{4}$$

where: $\overline{\sigma}$ is the true stress after considering damage; d_i is damage scalar, which can be expressed by damage evolution law, as shown in Eq. (5). The damage correlation can be iteratively applied to refine the true stress-strain relationship. This process involves adjusting the relationship in a manner that progressively aligns the finite element (FE) simulation outcomes with experimental data. By repeatedly applying the damage correlation in n-iteration, the model's predictive accuracy is enhanced, ensuring that the simulation results closely mirror the

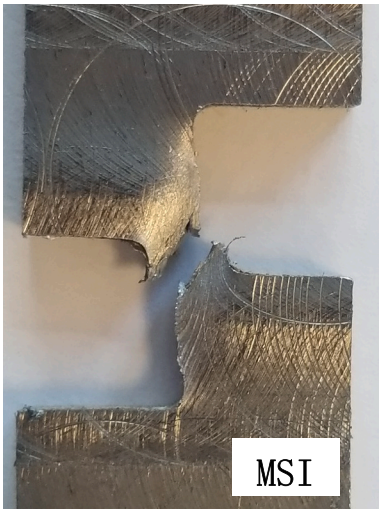

(a) 0^0 Directions

(b) 45^0 Directions

(c) 90^0 Directions

Fig. 15. Failure mode of milled double narrow notch specimens.

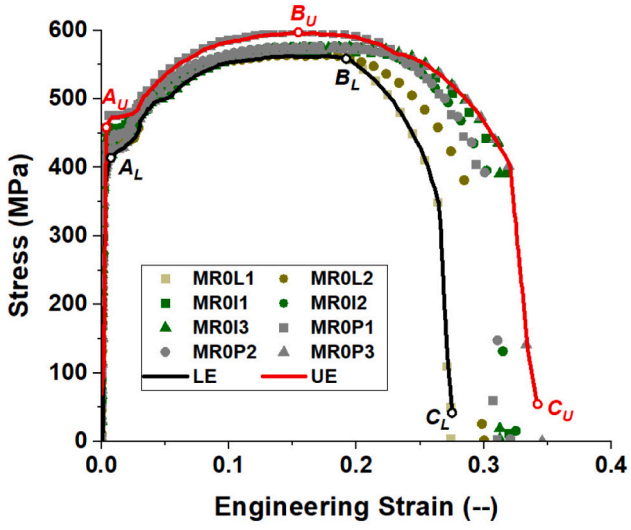

(a) Upper and lower envelope

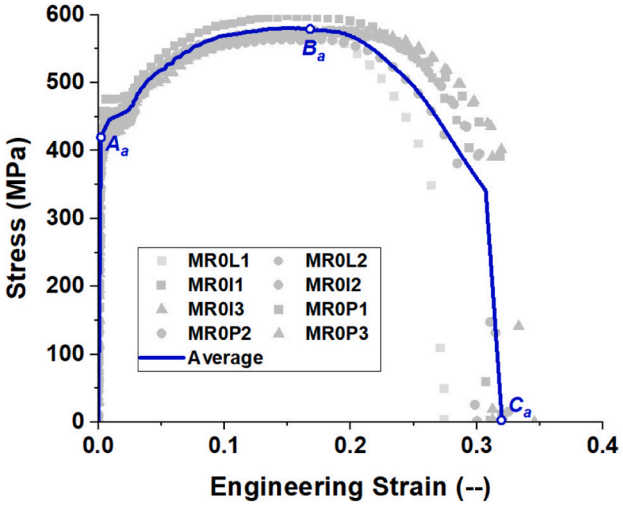

(b) Average line

Fig. 16. Upper, average and bottom line of engineering stress-strain curve for MR0 specimens.

observed material behaviour from testing.

$$d_i = \begin{cases} 0 & \bar{\varepsilon}^p < \bar{\varepsilon}^p_{d-i} \\ 1 - exp\left[- B_i\left(\bar{\varepsilon}^p - \bar{\varepsilon}^p_{d-i}\right) \right] & \bar{\varepsilon}^p \geq \bar{\varepsilon}^p_{d-i} \end{cases} \tag{5}$$

where: B_i is the parameter of damage evolution; $\bar{\varepsilon}^p_{d-i}$ is the corresponding plastic strain at the beginning of damage-dominated phase.

The parameters W and B_i, crucial for determining the true stress-strain relationship at different stages, are meticulously calibrated using a phased approach within the finite element (FE) framework. This systematic refinement ensures that the model's predictions are seamlessly synchronized with test data, providing a precise and reliable depiction of the material's mechanical response. During each calibration stage, as shown in Fig. 17, the finite element model is realistically modelled to mirror the boundary and load conditions of the actual test.

The engineering stress-strain curve, derived from the tensile test, serves as the benchmark for calibration. By systematically adjusting the values of the unknown parameters, the scattering between the finite element model's output and the engineering stress-strain curve is minimised to the best possible fit. This iterative process ensures that the

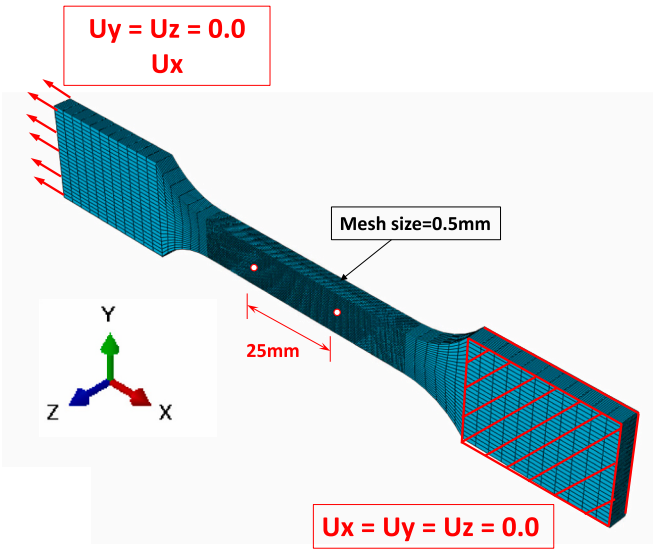

Fig. 17. The finite element model of milled dog-bone specimens [7].

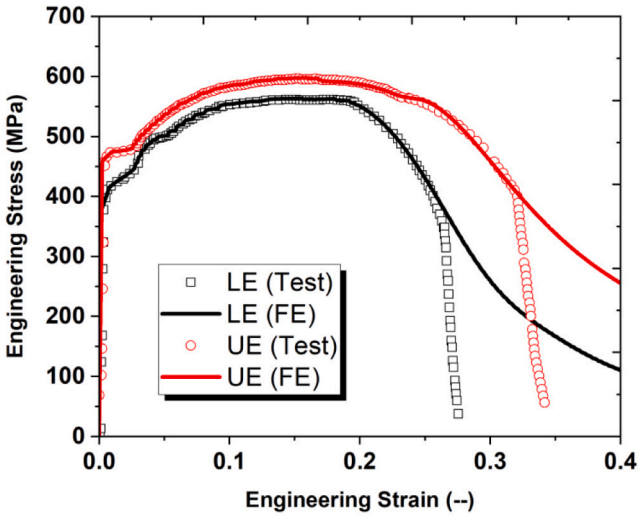

(a) Upper and lower envelope

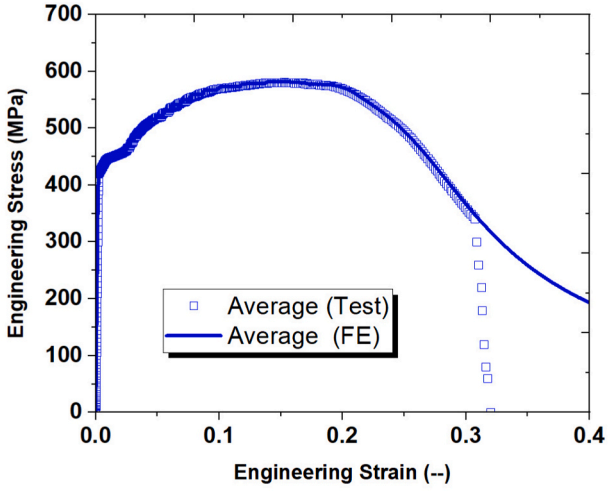

(b) Average line

Fig. 18. Comparison between FE calibrated results and MR0 specimens.

Table 13
Calibrated parameters for plastic-damage coupled phase.

Parameters	$\bar{\sigma}_u$	$\bar{\varepsilon}^p_u$	W	$\bar{\varepsilon}^p_{d-1}$	B_1	$\bar{\varepsilon}^p_{d-2}$	B_2
Unit	[MPa]	[−]	[−]	[−]	[−]	[−]	[−]
Upper Envelope	707.96	0.1808	0.3	0.5335	0.60	–	–
Lower Envelope	666.72	0.1731	0.0	0.2078	0.33	0.7730	0.07
Average line	684.71	0.1715	0.0	0.2342	0.22	0.3577	−0.18

model's predictions closely track the material's behaviour as observed in the tests, achieving a high degree of agreement in the simulation results. The optimal values for the unknown parameters in each stage are identified after attaining the closest proximity between the two curves—the finite element model's output and the experimental engineering stress-strain curve. This convergence signifies that the model has been successfully calibrated, capturing the material's response with low scattering across the various stages. The outcomes of the calibration process are succinctly presented in Fig. 18 and detailed in Table 13, providing a visual and tabular summary of the optimised parameter values.

3.1.2. Computational homogenization

From a microscopic perspective, the fracture failure in 3D printed steel is initiated by the nucleation of microscopic voids within the material. These voids subsequently grow and eventually coalesce, leading to the formation of macroscopic cracks that result in material rupture [21,34,35]. The representative volume element (RVE) of 3D printed steel can be conceptualized as a cubic structure, with a micro void centrally located within it. Consequently, a unit cubic cell featuring a spherical micro void at its core, as depicted in Fig. 19, is employed to symbolize the evolution of voids throughout the matrix deformation process. The porosity, which is 0.698 %, and the diameter of the spherical void within a unit cell are determined by analysing the chemical composition of the material, see [36] for detailed information. The relationship between the material's chemical makeup and the characteristics of the voids that form is provided by Eq. (6):

$$f_0 = 0.054\left[\%\mathrm{S}(wt) - \frac{10^{-3}}{\%\mathrm{Mn}(wt)}\right] + 0.055 \times \%\mathrm{O}(wt) \tag{6}$$

f_0 is the porosity of the unit cell; %S(wt), %Mn(wt) and %O(wt) represent the percentage content of sulfurt, manganese and oxygen in the material, respectively. The chemical composition of the 3D printed steel is given in [7].

Given the minimal void volume fraction in the initial stage, the constitutive relation serves as the matrix material model. Subsequently, the Hill-Mandel computational homogenization method [37] is employed to articulate the mesoscale relationship between the microscale and macroscale behaviour of the matrix material. This is based on the analysis of the unit cubic cell, as shown by Eq. (7).

$$\sigma_{ij} = \frac{1}{|\Theta|}\int_{\Theta} \widetilde{\sigma}_{ij} d\Theta \tag{7}$$

where: σ_{ij} represents macroscale Cauchy stress; $\widetilde{\sigma}_{ij}$ represents microscale Cauchy stress; Θ represents the unit cell domain.

By the virtual loading on the microscale unit cell, the behaviour of the matrix at the macroscale under a range of stress conditions can be effectively demonstrated. Mesoscale critical equivalent plastic strain (MCEPS), as measured on the void surface of the microscale unit cell, serves as an indicator of failure. It is assumed that this MCEPS value remains invariant for the unit cell, regardless of the multiaxial loading conditions to which the matrix is subjected [29,30]. Two proposed mesoscale indicators (MIs), see Eqs. (8) and (9), serve to predict failure using the Mesoscale Critical Equivalent Plastic Strain (MCEPS). Specifically, MI_1 is defined by the homogenised equivalent strain at the micro void surface, as the mesoscale failure index and MI_2 identifies the maximum equivalent strain at the micro void surface as the mesoscale failure index.

$$MI_1 = \frac{1}{|\Gamma_v|}\int_{\Gamma_v} \bar{\varepsilon}^p d\Gamma \tag{8}$$

$$MI_2 = max\left(_{\Gamma_v}\bar{\varepsilon}^p\right) \tag{9}$$

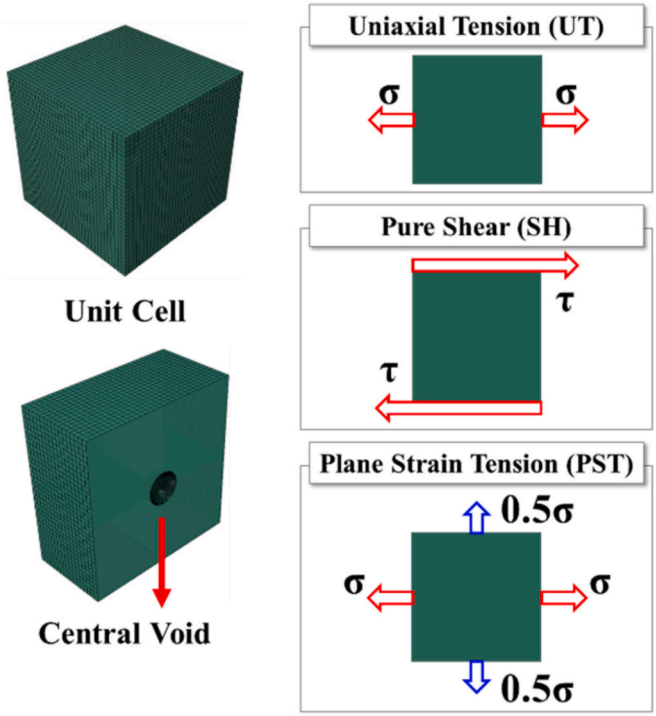

Fig. 19. RVE, cube cell with sphere void and virtual multiaxial loading.

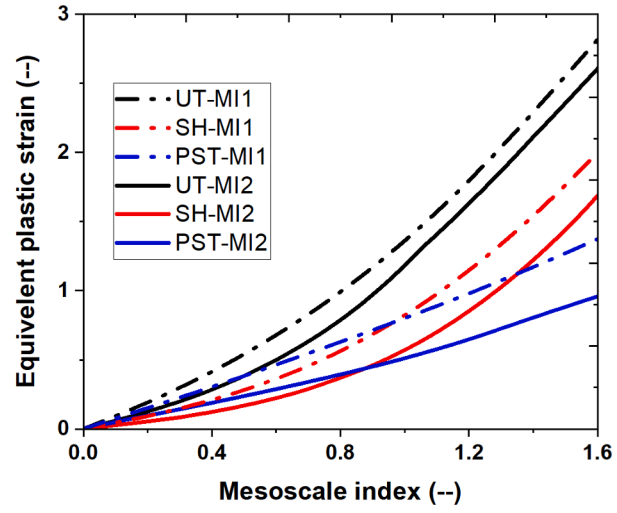

(a) Upper envelope

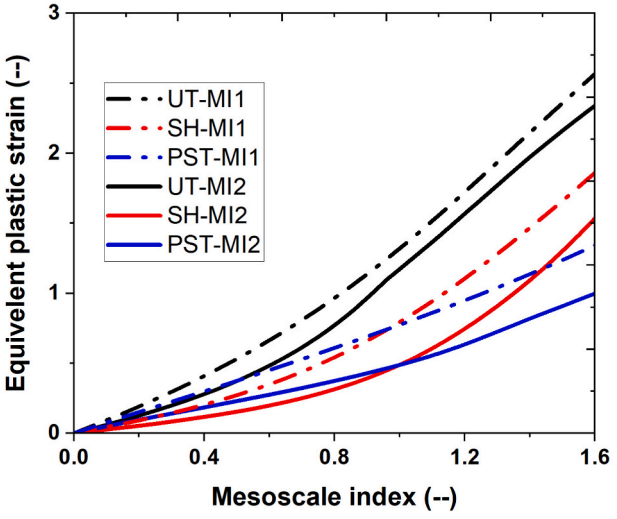

(b) Lower envelope

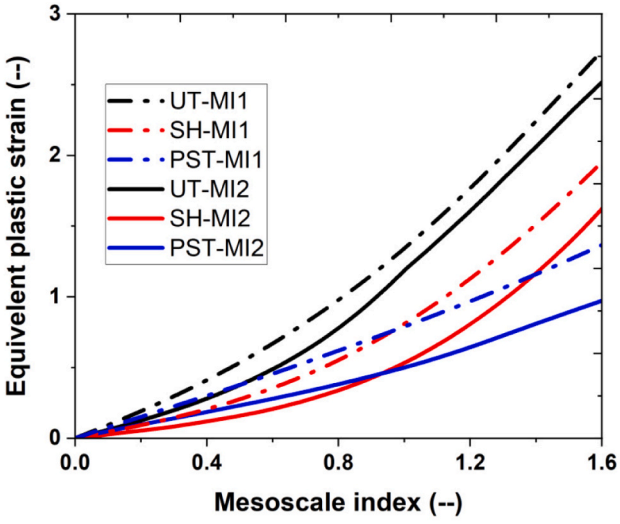

(c) Average line

Fig. 20. Mesoscale index (MI_2) vs. equivalent plastic strain (MI_2) for various loading on RVE.

Table 14
Equivalent plastic strain ratio related to uniaxial tension applied on REV.

Items		ξ_1	ξ_2	ξ_3	ξ_4	ξ_5	ξ_6	ξ_7
Upper envelope	MI_1 (SH/UT)	0.4611	0.0677	0.1364	−0.0628	−0.0902	0.0776	−0.0161
	MI_1(PST/UT)	0.8268	−0.0859	−0.6118	0.9150	−0.5533	0.1491	−0.0144
	MI_2 (SH/UT)	0.4129	−0.1088	0.6021	−0.6797	0.3087	−0.0481	0.0
	MI_2(PST/UT)	0.9961	−1.8926	3.6708	−4.2222	2.6196	−0.8074	0.00968
Lower envelope	MI_1 (SH/UT)	0.7471	−2.0824	5.7455	−7.0756	4.4151	−1.3492	0.1601
	MI_1(PST/UT)	0.9828	−1.6045	3.8215	−4.7460	2.9747	−0.9056	0.1067
	MI_2 (SH/UT)	0.4244	−0.0283	−0.0013	0.0171	−0.0131	0.0182	−0.0049
	MI_2(PST/UT)	0.9169	−1.2451	1.6945	−1.6041	0.9191	−0.2715	0.0316
Average line	MI_1 (SH/UT)	0.3981	0.2474	−0.1214	0.0536	−0.0110	0.0	0.0
	MI_1(PST/UT)	0.8756	−0.3540	−0.2132	0.8473	−0.8087	0.3294	−0.0494
	MI_2 (SH/UT)	0.3613	0.4975	−1.2003	1.3312	−0.7460	0.2238	−0.0293
	MI_2(PST/UT)	0.8238	−0.5290	−0.0475	0.3577	−0.1836	0.0294	0.0

where: Γ_v represents micro void surface. The MI evolutions along with the increase of macro equivalent plastic strain under different load conditions are shown in Fig. 20.

3.1.3. Fracture locus

Selected for its user-friendly parameter calibration, enhanced accuracy in predicting fractures, and extensive applicability, the uncoupled damage model known as the Lou-Huh model [17,38] is employed in this paper to pinpoint the fracture locus. The fracture strain within the damage model is given as a function of both stress triaxiality and the Lode angle parameter by Eq. (10).

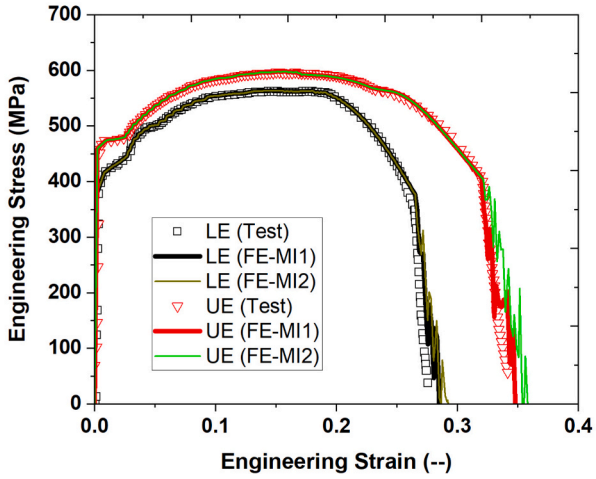

(a) Upper/lower envelope

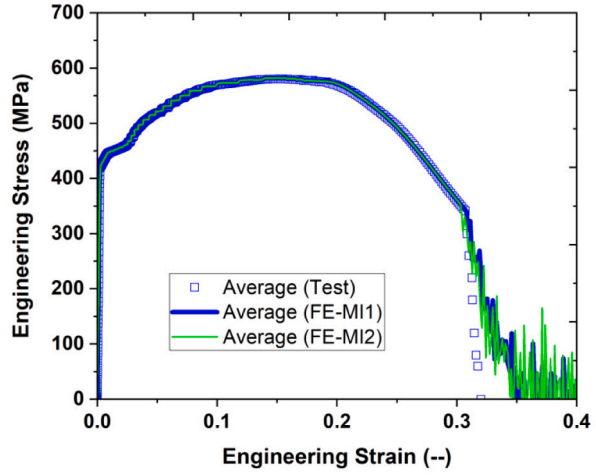

(b) Average line

Fig. 21. Calibrated results of stress-strain relation and fracture locus.

$$\bar{\varepsilon}_f^p = C_3\left(\frac{\sqrt{\bar{L}^2+3}}{2}\right)^{C_1}\left[\frac{1}{1+C}\left(\bar{\eta}+\frac{3-\bar{L}}{3\sqrt{\bar{L}^2+3}}+C\right)\right]^{-C_2} \tag{10}$$

where: $\bar{\eta}$ and $\bar{L}$ are the averaged stress triaxiality and averaged Lode angle parameter, which are averaged over loading history and shown in Eqs. (11) and (12). The stress triaxiality η and Lode angle parameter L are defined by principal stresses in Eqs. (13) and (14), C represents the cut-off value and is taken as 1/3, unknown parameters C_1, C_2 and C_3 can be calculated by Eqs. (15)–(17).

$$\bar{\eta} = \frac{1}{\bar{\varepsilon}_f^p}\int_0^{\bar{\varepsilon}_f^p} \eta d\bar{\varepsilon}^p \tag{11}$$

$$\bar{L} = \frac{1}{\bar{\varepsilon}_f^p}\int_0^{\bar{\varepsilon}_f^p} L d\bar{\varepsilon}^p \tag{12}$$

$$\eta = \frac{\frac{1}{3}(\sigma_1+\sigma_2+\sigma_3)}{\sqrt{\frac{1}{2}\left[(\sigma_1-\sigma_2)^2+(\sigma_2-\sigma_3)^2+(\sigma_1-\sigma_3)^2\right]}} \tag{13}$$

$$L = \frac{2\sigma_2-\sigma_1-\sigma_3}{\sigma_1-\sigma_3} \tag{14}$$

$$C_1 = log_{\left(\frac{2}{\sqrt{3}}\right)}\left[\frac{\bar{\varepsilon}_{UT}^p}{\bar{\varepsilon}_{SH}^p}\frac{(1/\sqrt{3}+C)}{(2/\sqrt{3}+C)}\right]^{-C_2} \tag{15}$$

Table 15
Calibrated parameters of fracture locus.

Item		C_1	C_2	C_3	$\bar{\varepsilon}_{UT}^p$	$\bar{\varepsilon}_{PST}^p$	$\bar{\varepsilon}_{SH}^p$
Lower envelope	MI_1	4.207	−0.156	1.100	1.100	0.611	0.566
	MI_2	7.343	0.029	1.200	1.200	0.416	0.422
Upper envelope	MI_1	6.550	0.120	1.500	1.500	0.577	0.612
	MI_2	9.731	0.544	1.700	1.700	0.395	0.516
Average line	MI_1	8.049	0.353	1.800	1.800	0.544	0.647
	MI_2	9.899	0.459	1.900	1.900	0.435	0.545

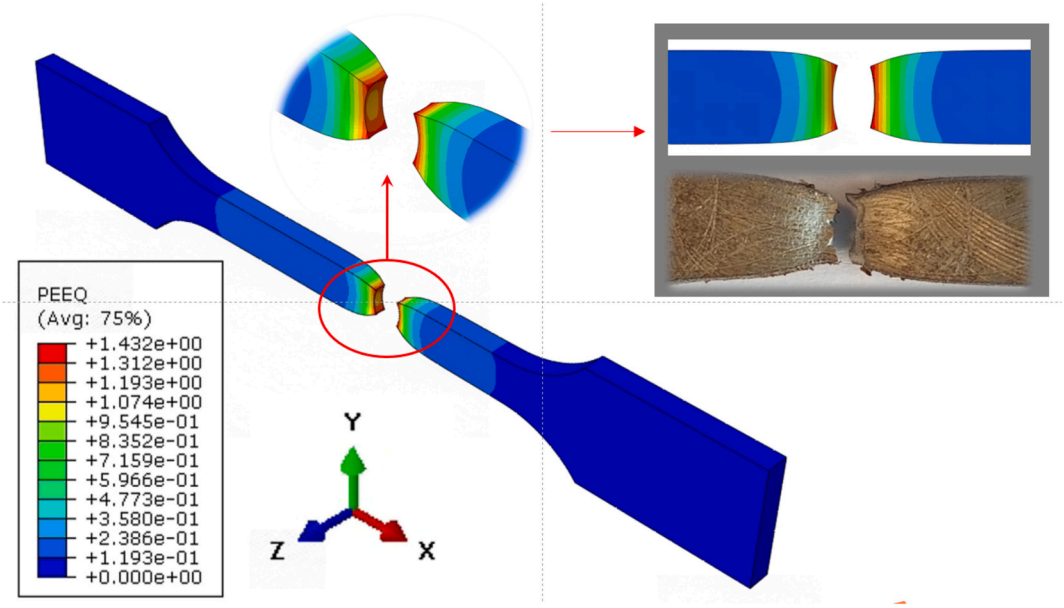

Fig. 22. Failure mode comparisons between FE and test of MR0 type specimens.

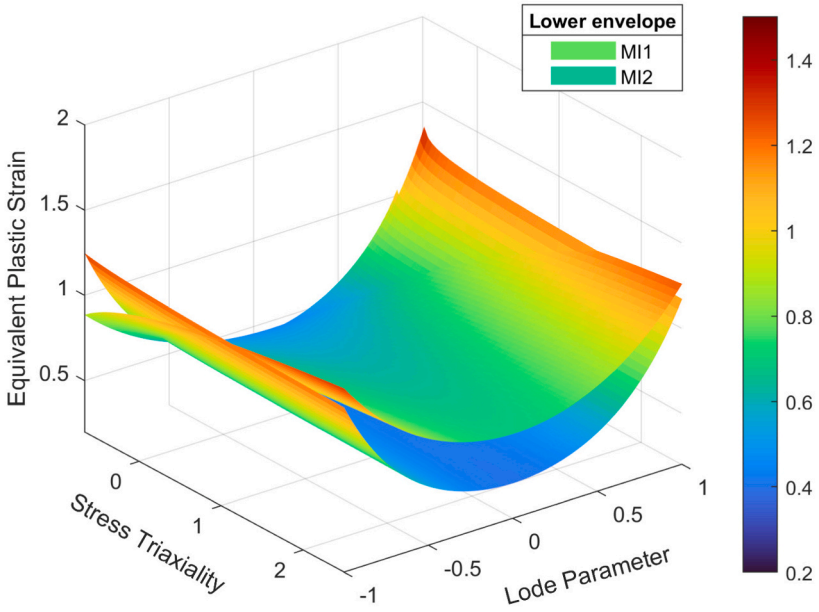

(a) Lower envelope

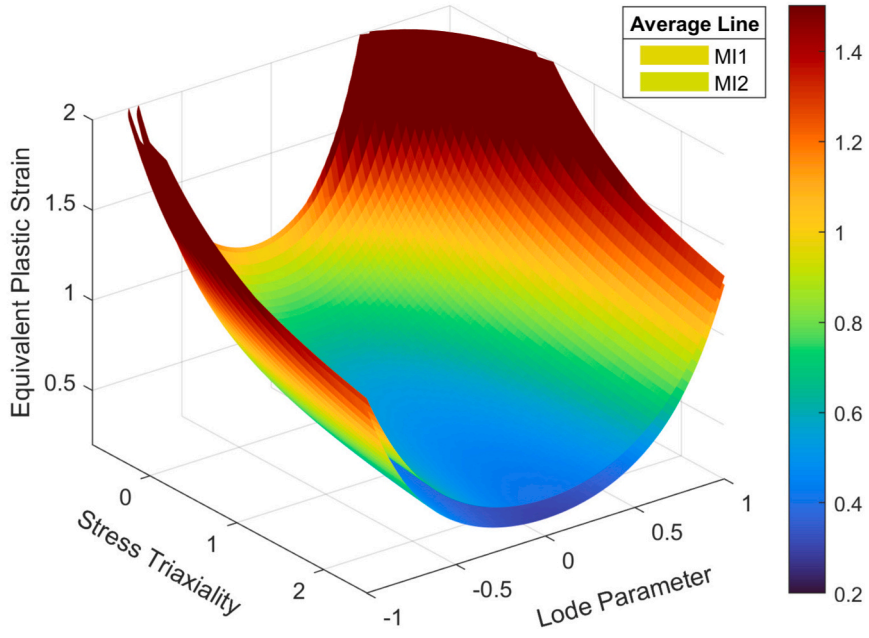

(b) Average line

Fig. 23. Equivalent plastic strain to fracture depending on stress triaxiality and lode parameter.

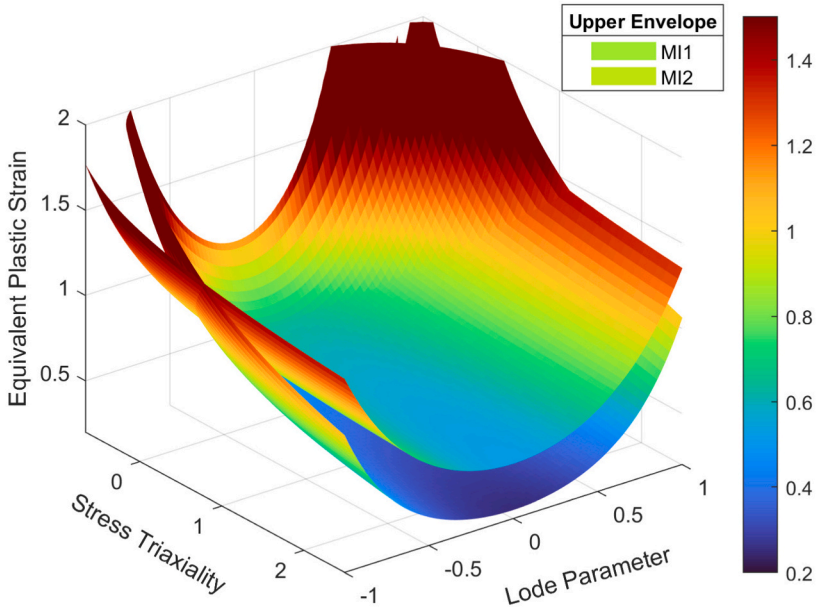

(c) Upper envelope

Fig. 23. (*continued*).

$$C_2 = log\left(\frac{1/\sqrt{3}+C}{2/\sqrt{3}+C}\right)\left(\frac{\bar{\varepsilon}^p_{PST}}{\bar{\varepsilon}^p_{SH}}\right) \tag{16}$$

$$C_3 = \bar{\varepsilon}^p_{UT} \tag{17}$$

In Eqs. (15)–(17), the equivalent fracture plastic strain exposed to uniaxial tensile (*UT*), pure shear (SH) and plane strain tension (PST) are unknown, and named $\bar{\varepsilon}^p_{UT}$, $\bar{\varepsilon}^p_{SH}$, $\bar{\varepsilon}^p_{PST}$, respectively. Three virtual loadings are independently applied to the unit cell, see Fig. 19, to get the relationship between the equivalent strain of fracture under different stress states in the microscale of the matrix. The relations between strain ratio and fracture strain exposed to uniaxial tensile are fitted by seven-term polynomial equations, see Eq. (18).

$$r_x = \sum_{i=1}^{7} \xi_i \left(\bar{\varepsilon}^p_{UT}\right)^{i-1} \quad x = \{SH/UT, PST/UT\} \tag{18}$$

where: r_x represents fracture plastic strain ratio between SH or PST and UT; ξ_i is the fitting coefficient of the polynomial. The coefficients of the seven-term polynomial are shown in Table 14.

For Eqs. (15)–(17), parameter $\bar{\varepsilon}^p_{UT}$ is determined by the calibration of finite element model based on the milled dog-bone specimens, the ratio of $\bar{\varepsilon}^p_{UT}/\bar{\varepsilon}^p_{SH}$ and $\bar{\varepsilon}^p_{PST}/\bar{\varepsilon}^p_{SH}$ is obtained by Eq. (18), then the fracture locus using Eq. (10) is identified. The calibrated results of the stress-strain relation and fracture locus under uniaxial tensile load are shown in Fig. 21 for the upper and lower envelop. After calibrating the fracture parameters, the calibrated engineering stress-strain relation is in good agreement with the experimental coupon results. Fig. 22 illustrates a very good agreement of the failure modes obtained in MR0 type specimen, and the results from finite element (FE) analysis.

The summary of calibrated parameters of the fracture locus is concisely presented in Table 15. The equivalent plastic strain to fracture as calibrated by the average MCEPS MI_1, is smaller than the value calibrated from maximum MCEPS MI_2. The equivalent plastic strain to fracture depending on the stress triaxiality and lode parameters is shown in Fig. 23. For lower envelope and average line, the equivalent plastic strain to fracture surface from *MI2* is higher than from one obtained by *MI1*. For the lower envelope, the surface of the equivalent plastic strain to fracture, calibrated by *MI2*, is greater than that of *MI1*. For the upper envelope, the surface corresponding to the equivalent plastic strain at fracture, calibrated by *MI2*, intersects with the surface calibrated by *MI1*.

3.2. Validation of ductile fracture simulation

3.2.1. Description of finite element model

The finite element model used for the verification of the calibrated parameters, is shown in Fig. 24. Typically, the coupon specimen model has prevented displacement at one end while the displacement is applied on the opposite end. The specimen is modelled using solid elements C3D8 [39]. The quasi-static simulation is conducted with the ABAQUS/EXPLICIT solver, which spans a total duration of 1 s using appropriate mass scaling (1×10^{-5} s). It should be noted that the time step duration does not have a physical significance in this context. The time increment is set at 1×10^{-5} s. Engineering stress is determined by the ratio of the nominal force to the smallest cross-sectional area along the specimen's length. The definition of engineering strain encompasses the ratio of the displacement increment to the original gauge length of the specimen. The original gauge length for different specimens is shown in Fig. 24.

3.2.2. Comparisons between FE simulation and test results

3.2.2.1. Milled double notch specimens. The comparison of the engineering stress-strain relationships for MR3 type specimens between FE analysis and experimental tests is shown in Fig. 25 for the upper and lower bounds, and in Fig. 26 for the mean curve. The results from varying MCEPS parameters lead to different fracture displacements. Generally, the FE predictions based on parameters calibrated using the average MCEPS (MI_1) align more closely with the experimental data than those based on the maximum MCEPS (MI_2). Furthermore, the simulation of specimens with varying widths is conducted to reflect the actual experimental conditions, as the fractured specimens exhibit different widths. The results showed that the width of the specimens

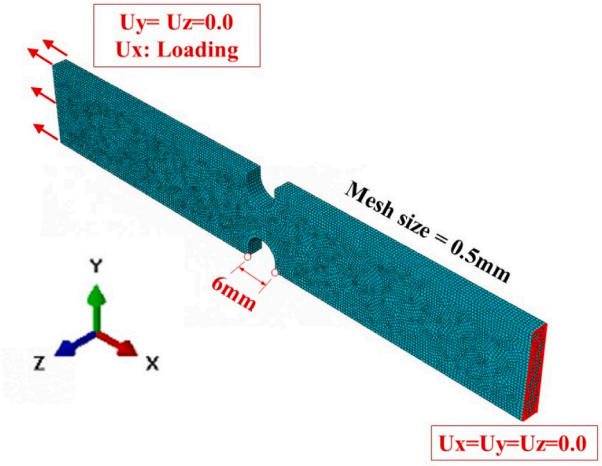

(a) MR3 specimen

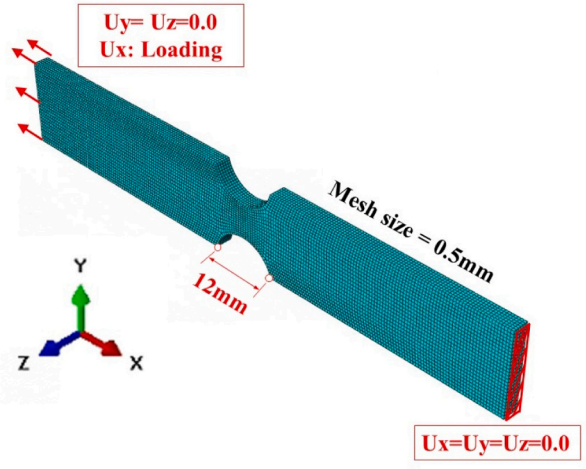

(b) MR6 specimen

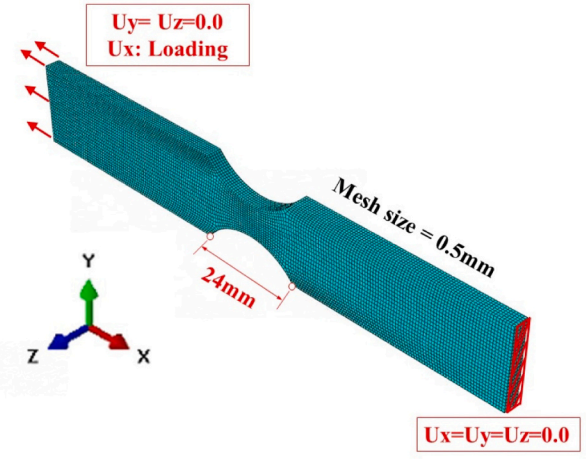

(c) MR12 specimen

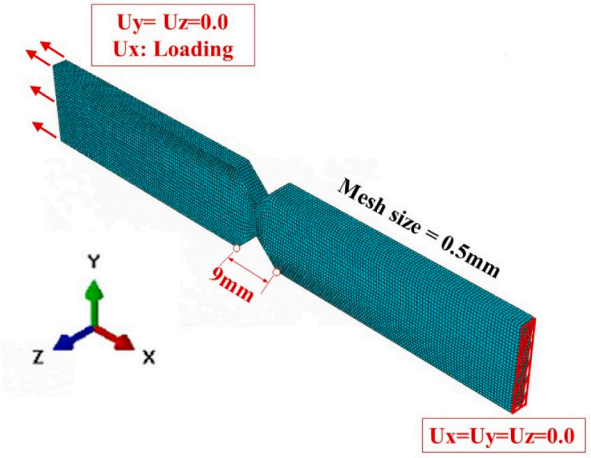

(d) MRV specimen

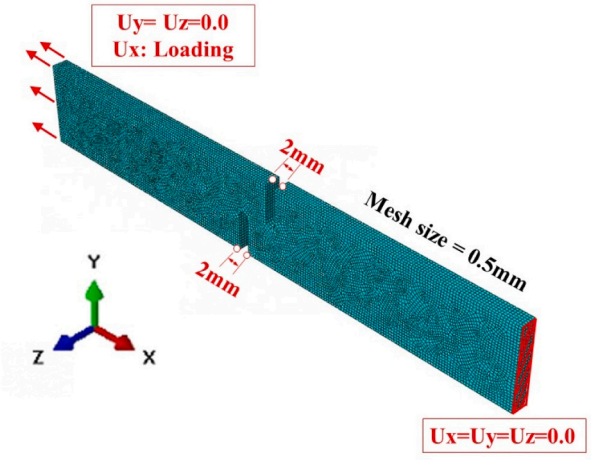

(d) MSI specimen

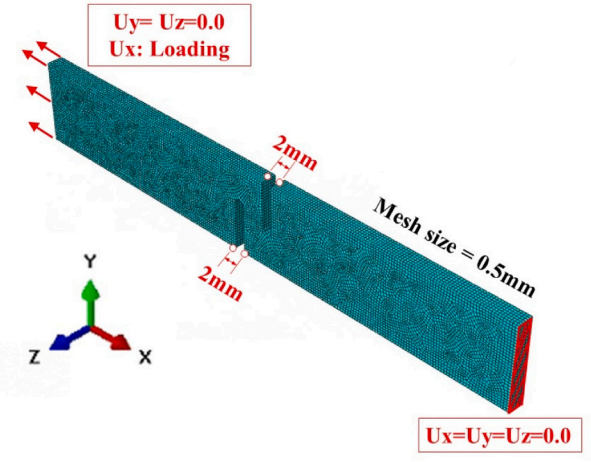

(e) MSII specimen

Fig. 24. Calibrated results of stress-strain relation and fracture locus.

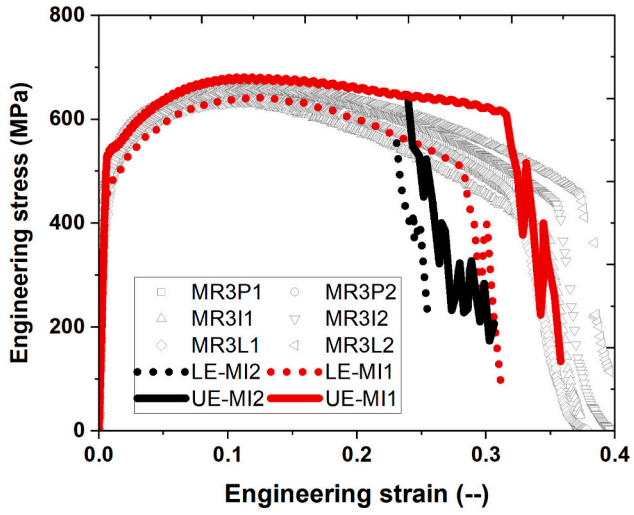

(a) MR3 specimen (W=15mm)

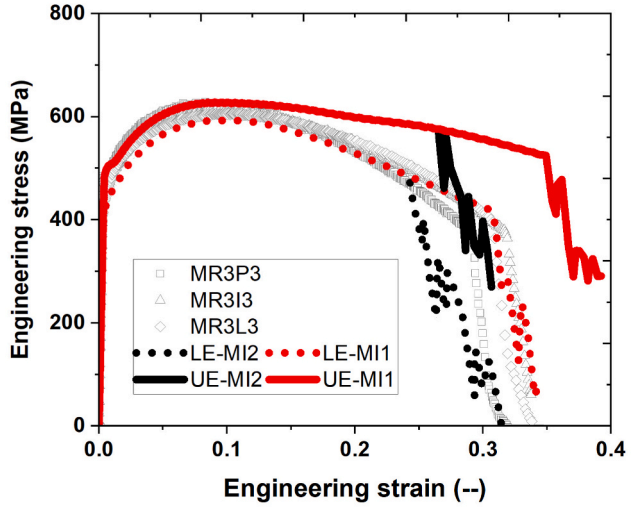

(b) MR3 specimen (W=10mm)

Fig. 25. Upper and lower engineering stress-strain relationship comparisons of MR3 between FE and tests.

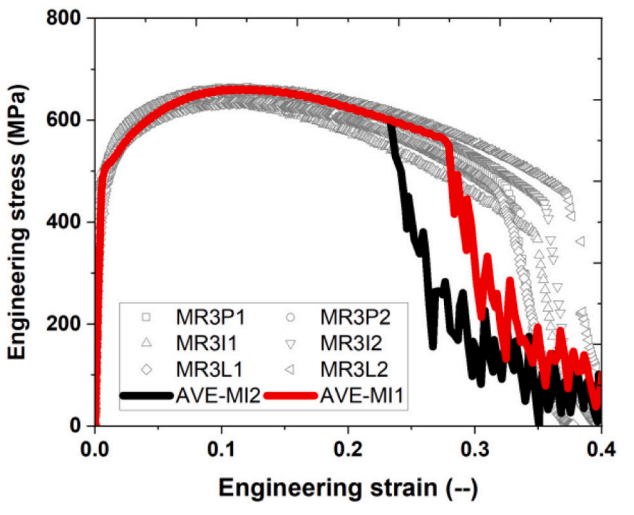

(a) MR3 specimen (W=15mm)

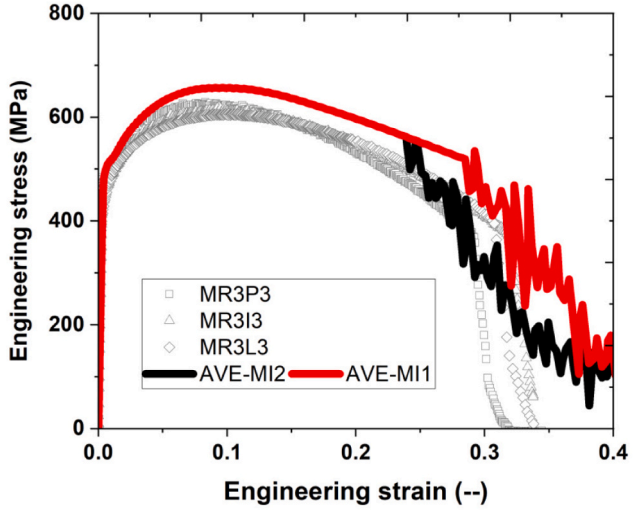

(b) MR3 specimen (W=10mm)

Fig. 26. Average engineering stress-strain relationship comparisons of MR3 between FE and tests.

significantly influences the fracture displacement; wider specimens tend to exhibit a higher fracture engineering strain.

The comparison of failure modes between FE predictions and experimental results is presented in Fig. 27a. The failure mode is largely consistent with the experimental observations, with the exception of four elongated elements obtained from the corners of the printed steel plates. The fracture pattern observed in the Finite Element (FE) simulation is not smooth, primarily attributed to the influence of mesh size, and different equivalent plastic strain to fracture varied with the stress triaxiality and Lode angle parameter.

The engineering stress-strain relationship of the MR6 specimens obtained by finite element (FE) analysis and experimental results are presented in Fig. 28, with the upper and lower bounds for specimens of various widths. The average engineering stress-strain relationship comparisons between FE analysis and tests are illustrated in Fig. 29. Additional simulations are conducted of a specimen width of 13 mm to investigate possible differences caused by specimens cut very closely to it. For specimens with widths of 15 mm and 13 mm, the experimentally observed fracture displacement falls within the range defined by the upper and lower bounds of the finite element (FE) results, which were predicted using the maximum MCEPS (MI_2) parameters. It is noted that in some cases, the stress-strain relationships are outside these boundaries. This discrepancy indicated that the number of repetitions in dog-bone specimens should be increased to comprehend better the "natural" variability in the properties of isolated plates manufactured by WAAM. The need for additional testing underscores the importance of thorough characterisation to account for the material's scatter and to enhance the accuracy of FE models in predicting mechanical behaviour. However, the finite element (FE) predictions, when calibrated with the average MCEPS (*MI1*), align more closely with the test results for a specimen width of 13 mm than those calibrated with the maximum MCEPS (*MI2*). For 15 mm width, the trend is reversed, with the maximum MCEPS (*MI2*) predictions showing better agreement with experimental data. The comparison of failure modes between FE predictions and experimental tests is depicted in Fig. 27b.

One source of uncertainty is related to the influence of the manufacturing process, which is left out of the objectives of this paper.

The failure mode is generally consistent with experimental observations. A 'sawtooth' pattern of failure is noted in the FE predictions, which deviates from the experimental findings. This discrepancy could be mitigated by employing a finer mesh size; however, doing so would significantly extend the computational time.

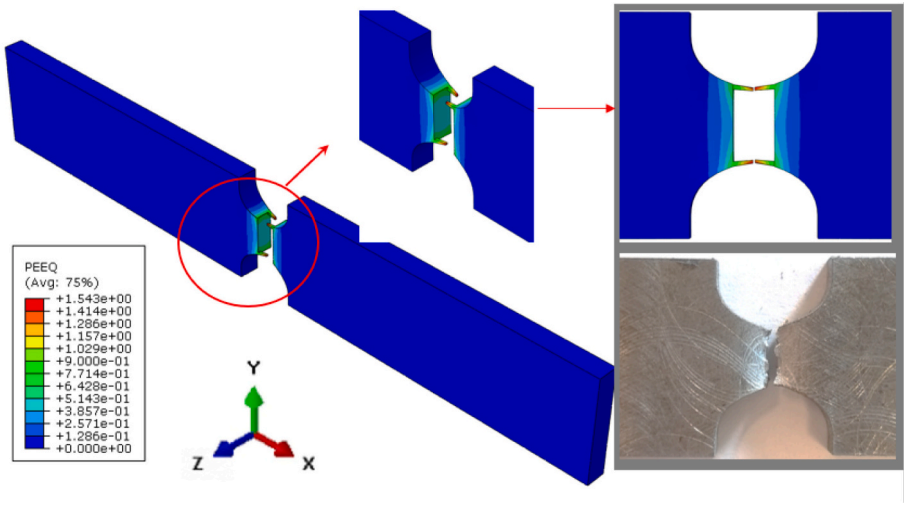

(a) MR3 specimens

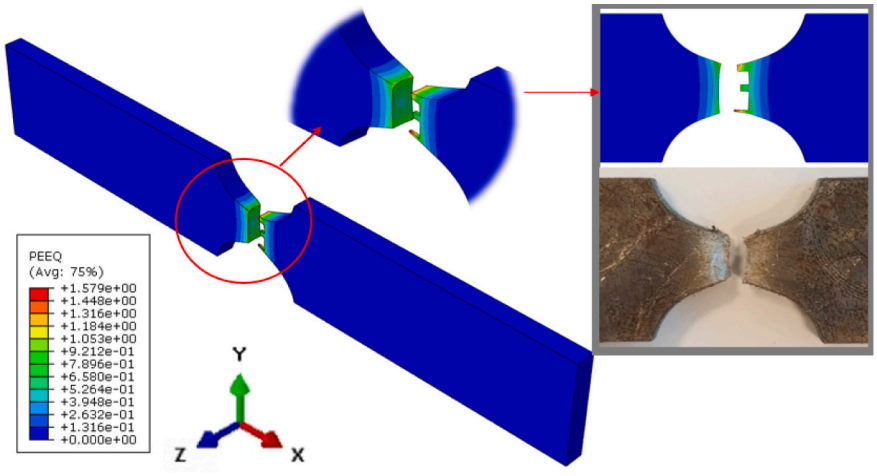

(b) MR6 specimens

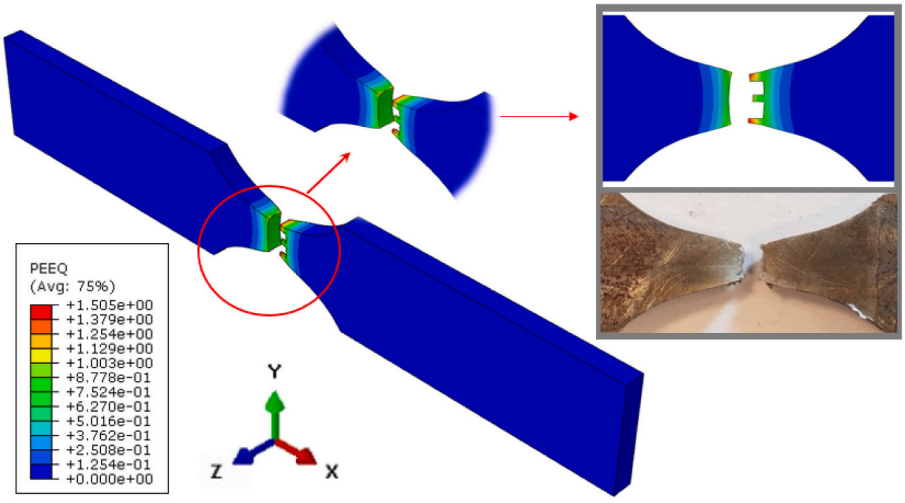

(c) MR12 specimens

Fig. 27. Failure mode comparisons of MR type specimens between FE and test.

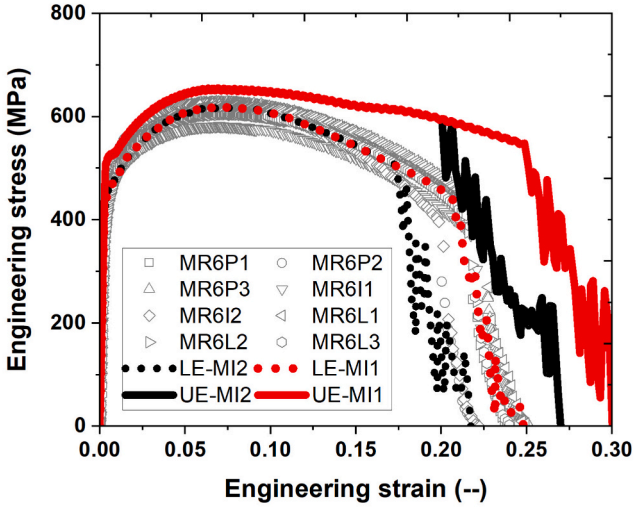

(a) MR6 specimen (W=15mm)

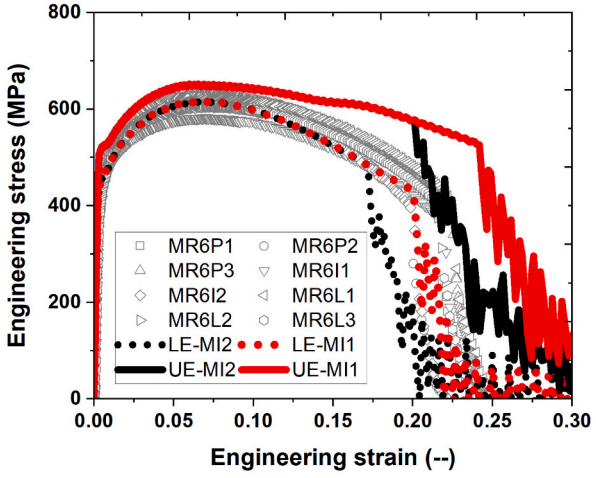

(b) MR6 specimen (W=13mm)

Fig. 28. Upper and lower engineering stress-strain relationship comparisons of MR6 between FE and tests.

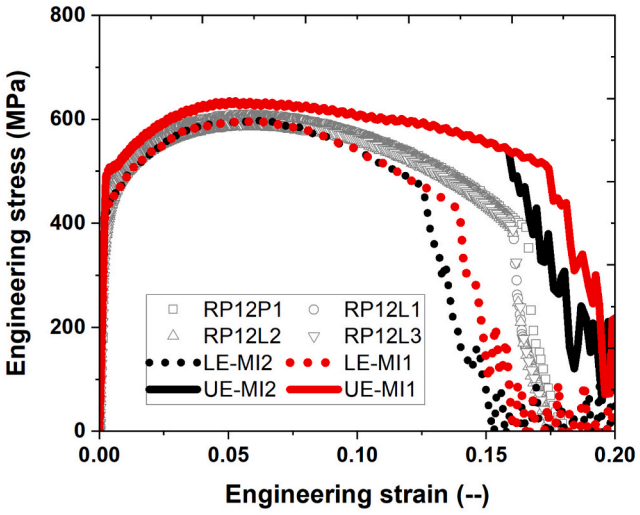

(a) Upper and lower envelope

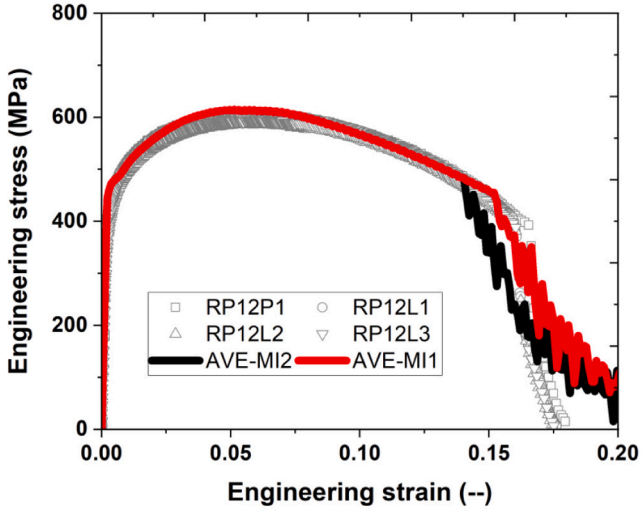

(b) Average line

Fig. 30. Engineering stress-strain relationship comparisons of MR12 between FE and tests.

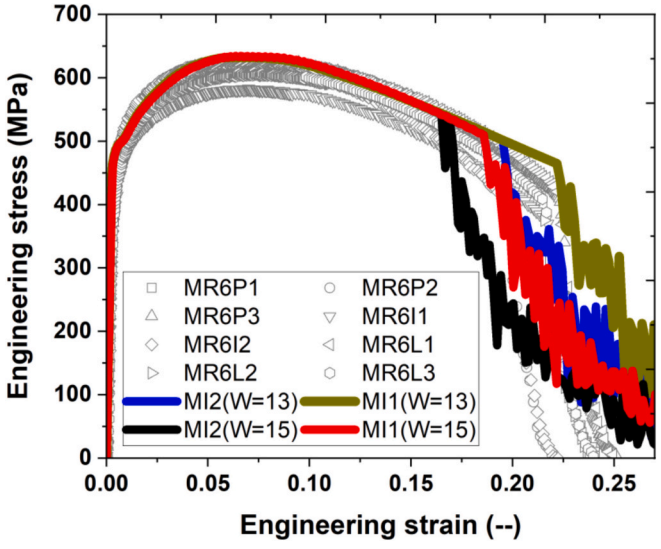

Fig. 29. Average engineering stress-strain relationship comparisons of MR6 between FE and tests.

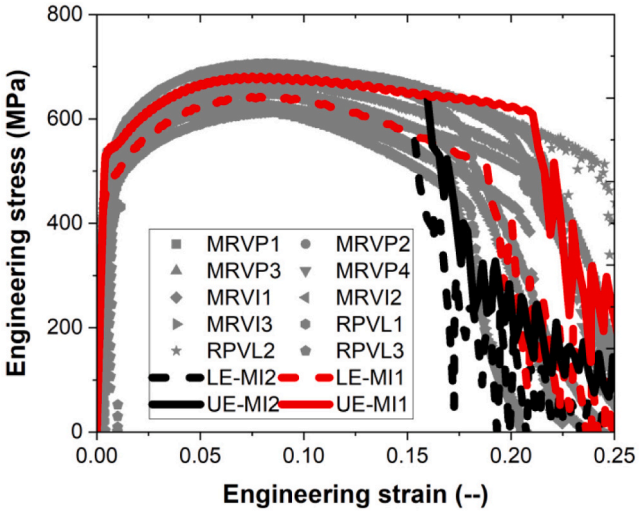

(a) Upper and lower envelope

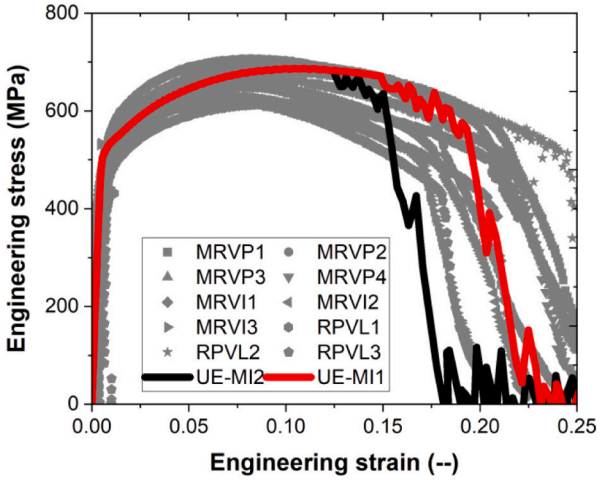

(b) Average line

Fig. 31. Engineering stress-strain relationship comparisons of MRV between FE and tests.

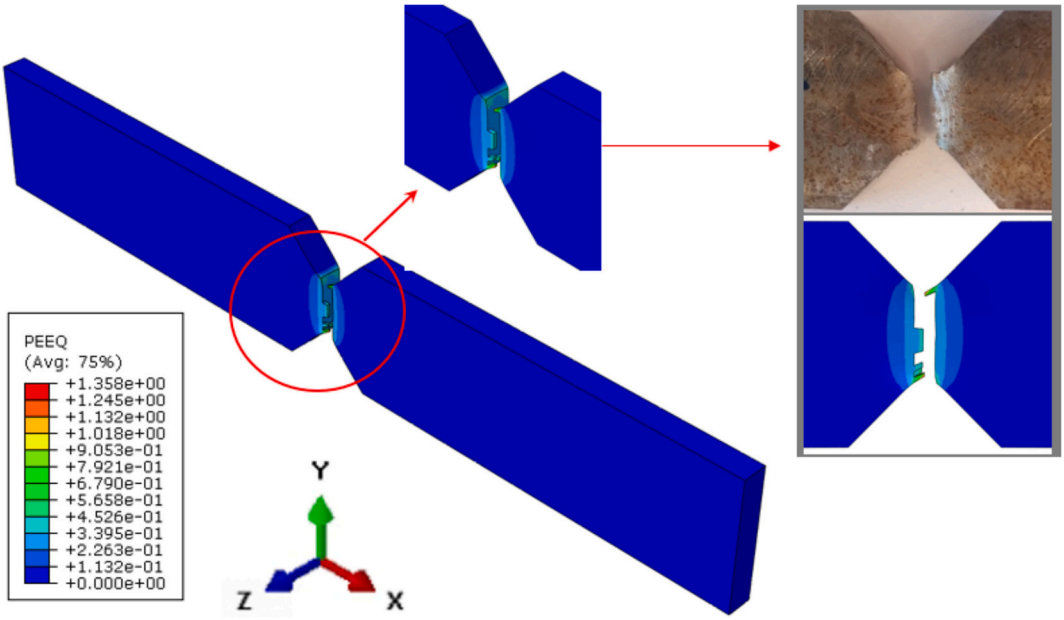

Fig. 32. Failure mode comparisons of MRV type specimens between FE and test.

Results of FE analysis and experiments are compared in Fig. 30. In Fig. 30a, the experimental results for MR12 specimens fall within the upper and lower bounds defined by the average MCEPS (*MI1*) and the maximum MCEPS (*MI2*). The FE predictions calibrated with average MCEPS (MI_1) and maximum MCEPS (MI_2) agree with the test outcomes. The discrepancy between the FE predictions based on average and maximum MCEPS is minimal. This is likely due to the stress state of MR12 being close to the uniaxial tension, with both sets of simulations calibrated using dog-bone specimens. The comparison of failure modes between finite element (FE) predictions and experimental tests is depicted in Fig. 27c. The failure mode is generally consistent with experimental observations, except for the 'sawtooth' pattern along the cross-sections, which may be attributed to mesh size effects.

3.2.2.2. Milled double sharp notch specimens. Fig. 31 compares the engineering stress-strain relationships for MRV specimens, as determined by finite element (FE) analysis and experimental tests. Ten tests were conducted on the MRV specimens, yielding test data that is more redundant than that of other specimen types. Consequently, the scatter in the test results for MRV specimens is comparatively greater, with the bounds of experimental outcomes even exceeding those predicted by finite element (FE) simulations. Among the finite element (FE) predictions, those calibrated with the average MCEPS (MI_1) show a closer alignment with test observations across both the upper and lower bound predictions and the average lines, compared to those based on the maximum MCEPS (MI_2). The comparison of failure modes for MRV specimens between FE analysis and experimental tests is depicted in Fig. 32. The predicted failure mode of the MRV specimens is consistent with the experimental observations.

3.2.2.3. Milled double narrow notch specimens. The comparison of the engineering stress-strain relationship for MSI specimens, as determined by finite element (FE) analysis and experimental data, is illustrated in Fig. 33. Notably, there is a pronounced difference between FE predictions and experimental observations, particularly for MSI specimens. This discrepancy is attributed to manufacturing constraints, which have resulted in actual specimen widths deviating from the design specifications, with widths ranging from 14.0 mm to 15.0 mm. The influence of specimen width on the engineering stress-strain relationship for MSI specimens was investigated using FE predictions. The findings indicate that the width significantly affects the curve's shape. This is because the gauge length for MSI specimens is "arbitrary" (without the physical meaning), taken as 2 mm, and even slight variations in displacement increments causes considerable differences in the stress-strain response. The experimental results are found to align with the predictions for the 15 mm and 13.5 mm wide specimens. To enhance the predictive accuracy of the engineering stress-strain relationship, it is imperative to develop a more sophisticated model in the future. This refined model should take into account the complexity of the manufacturing process and the material properties depending on it.

The engineering stress-strain relationship for MSII specimens is shown in Fig. 34, where the agreement of results obtained from finite element (FE) simulations and experimental measurements is shown. The fracture displacements predicted by both the maximum MCEPS (MI_2) and the average MCEPS (MI_1) are consistently lower than those observed in the experimental outcomes. Notably, the predictions derived from the average MCEPS (MI_1) align more closely with the test data compare with those from the maximum MCEPS (MI_2). In terms of ultimate engineering stress, the discrepancies between the predicted and experimental values are acceptable, with a margin of 25 % for the UE/LE envelope and 15 % for the average line. The large strain difference is mainly due to 2 mm gauge length. The failure mode comparisons of MS specimens between FE and test are shown in Fig. 35. The predicted failure modes for both MSI and MSII specimens are in good agreement with experimental observations.

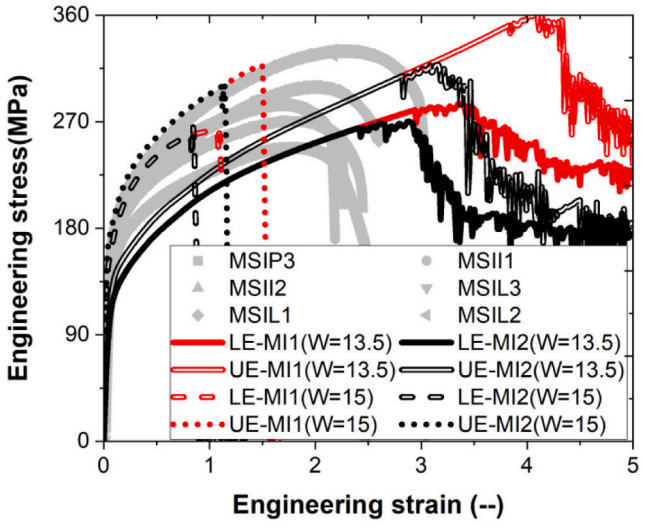

(a) Upper and lower envelope

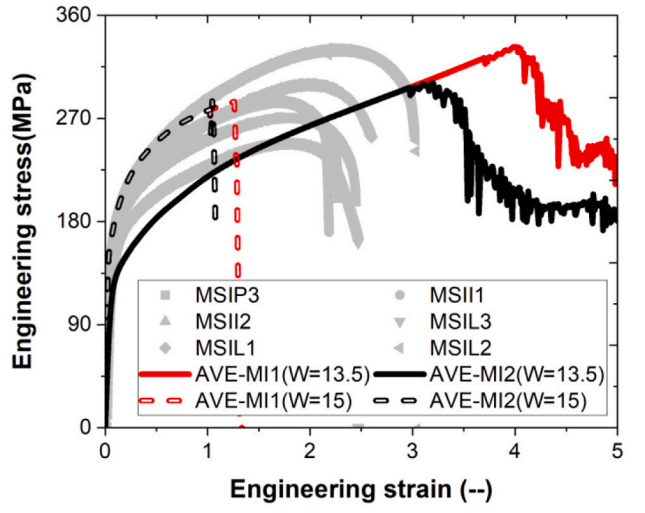

(b) Average line

Fig. 33. Engineering stress-strain relationship comparisons of MSI between FE and tests.

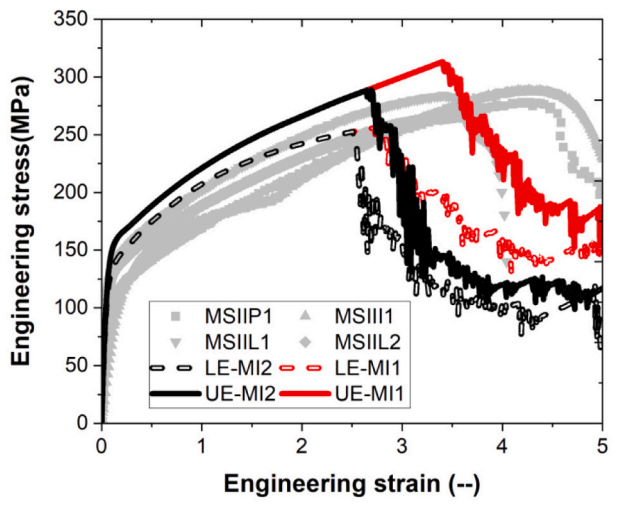

(a) Upper and lower envelope

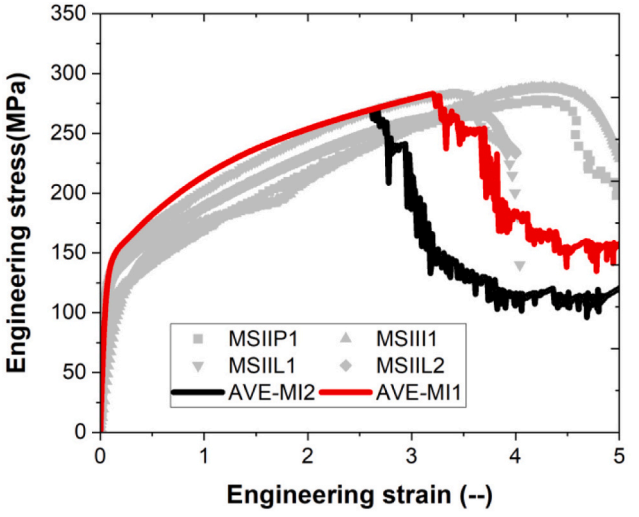

(b) Average line

Fig. 34. Engineering stress-strain relationship comparisons of MSII between FE and tests.

4. Conclusion

A comprehensive study investigated the ductile fracture characteristics of steel plates manufactured via the GMAW process. The ductile fracture behaviour of WAAM steel is predicted by the mesoscale equivalent plastic strain (MSCEPS) approach. The following conclusions can be drawn:

(1) Specimens' cut is oriented to 0° (parallel to the main printing layer), 45° (inclined), and 90° (perpendicular to the main printing layer), to systematically evaluate the material's anisotropic behaviour. Differences are observed among specimens in various orientations, but the variations attributed to orientation are relatively minor compared to the scattering of results from the same batch of materials. Consequently, the anisotropic properties of the WAAM steel plates may be considered negligible.

(2) In reviewing the impact of surface roughness on material properties, in addition to the yield strength in the direction perpendicular to the printing axis, the variations of elastic modulus, ultimate strength, and uniform elongation, are considered negligible, as they are overshadowed by the inherent variability within the same production batch.

(3) The accuracy of the calibrated parameters is validated by comparing the engineering stress-strain relationships obtained from experimental tests and finite element (FE) analysis. Generally, the finite element (FE) predicted results derived from the average MCEPS (*MI1*) tend to give better agreement with experimental observations than those from the maximum MCEPS (*MI2*). Tables 13 and 15 list all the material parameters utilized in the uncoupled ductile fracture simulations for a mesh size of 0.5 mm.

CRediT authorship contribution statement

Haohui Xin: Formal analysis, Investigation, Methodology, Resources, Software, Writing – original draft. **Junqiang Li:** Formal analysis, Investigation. **Youyou Zhang:** Formal analysis, Validation, Writing – review & editing. **Milan Veljkovic:** Funding acquisition, Supervision, Writing – review & editing. **Nicolas Persem:** Writing – review & editing, Project administration. **Laurent Lorich:** Project administration, Writing – review & editing.

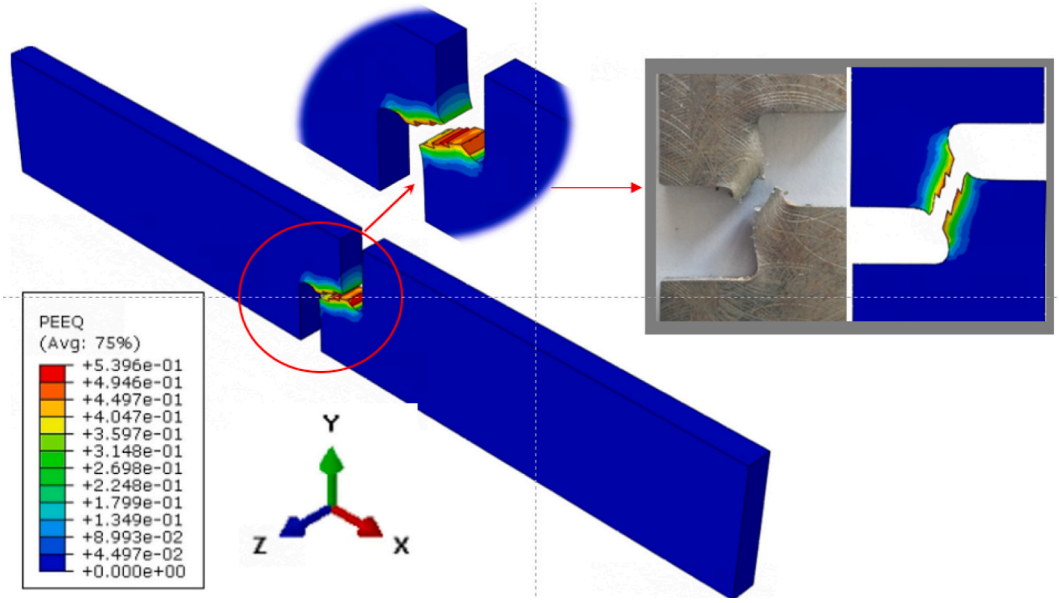

(a) MSI type specimens

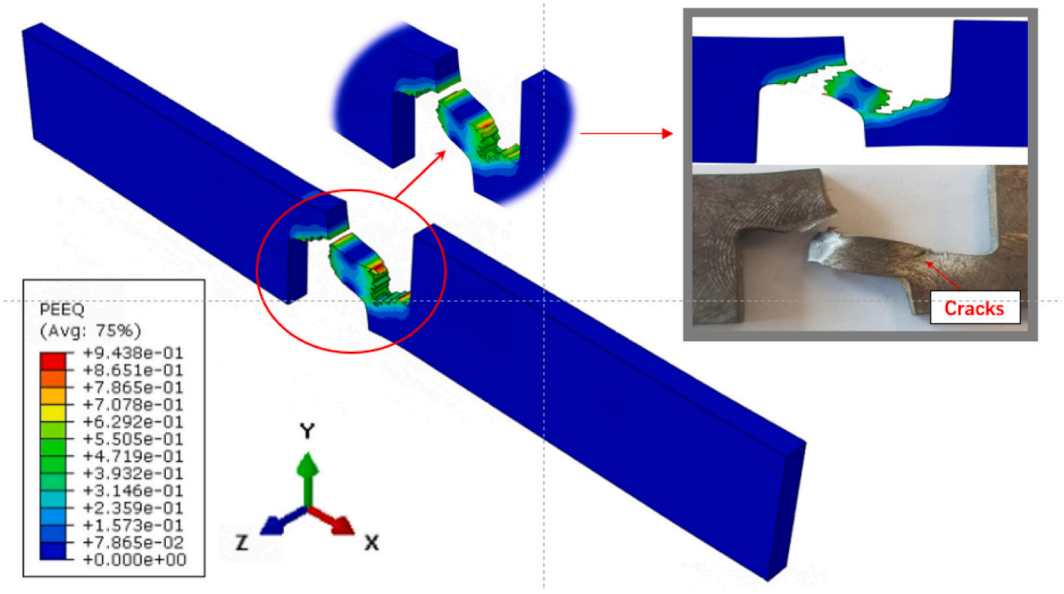

(b) MSII type specimens

Fig. 35. Failure mode comparisons of MS type specimens between FE and test.

Declaration of competing interest

The authors declare that they have no known competing financial interests or personal relationships that could have appeared to influence the work reported in this paper.

Data availability

Data will be made available on request.

References

[1] C.R. Cunningham, J.M. Flynn, A. Shokrani, V. Dhokia, S.T. Newman, Invited review article: strategies and processes for high quality wire arc additive manufacturing, Addit. Manuf. 22 (2018) 672–686.

[2] B. Wu, Z. Pan, D. Ding, D. Cuiuri, H. Li, J. Xu, J. Norrish, A review of the wire arc additive manufacturing of metals: properties, defects and quality improvement, J. Manuf. Process. 35 (2018) 127–139.

[3] S. Anderson Goehrke, 3D Printed Steel Pedestrian Bridge Will Soon Span an Amsterdam Canal, 3D Print, 2015.

[4] L. Gardner, P. Kyvelou, G. Herbert, C. Buchanan, Testing and initial verification of the world's first metal 3D printed bridge, J. Constr. Steel Res. 172 (2020) 106233.

[5] J. Lange, T. Feucht, M. Erven, 3D printing with steel: additive manufacturing for connections and structures, Steel Constr. 13 (2020) 144–153.

[6] T. Feucht, J. Lange, B. Waldschmitt, A.-K. Schudlich, M. Klein, M. Oechsner, Welding process for the additive manufacturing of cantilevered components with the WAAM, in: Adv. Join. Process, Springer, 2020, pp. 67–78.

[7] H. Xin, I. Tarus, L. Cheng, M. Veljkovic, N. Persem, L. Lorich, Experiments and numerical simulation of wire and arc additive manufactured steel materials, Structures 34 (2021) 1393–1402, https://doi.org/10.1016/j.istruc.2021.08.055.

[8] C.V. Haden, G. Zeng, F.M. Carter III, C. Ruhl, B.A. Krick, D.G. Harlow, Wire and arc additive manufactured steel: tensile and wear properties, Addit. Manuf. 16 (2017) 115–123.

[9] L. Sun, F. Jiang, R. Huang, D. Yuan, C. Guo, J. Wang, Anisotropic mechanical properties and deformation behavior of low-carbon high-strength steel component fabricated by wire and arc additive manufacturing, Mater. Sci. Eng. A . 787 (2020) 139514.
[10] A. Ermakova, A. Mehmanparast, S. Ganguly, J. Razavi, F. Berto, Investigation of mechanical and fracture properties of wire and arc additively manufactured low carbon steel components, Theor. Appl. Fract. Mech. 109 (2020) 102685.
[11] P. Kyvelou, H. Slack, D.D. Mountanou, M.A. Wadee, T. Ben Britton, C. Buchanan, L. Gardner, Mechanical and microstructural testing of wire and arc additively manufactured sheet material, Mater. Des. 192 (2020) 108675.
[12] T.T. Vittoria Laghi, Michele Palermo, Giada Gasparini, Milan Veljkovic, Assessment of design mechanical parameters and partial safety factors for wire-and-arc additive manufactured stainless steel, Eng. Struct. 225 (2020) 11314.
[13] B.A. Szost, S. Terzi, F. Martina, D. Boisselier, A. Prytuliak, T. Pirling, M. Hofmann, D.J. Jarvis, A comparative study of additive manufacturing techniques: residual stress and microstructural analysis of CLAD and WAAM printed Ti–6Al–4V components, Mater. Des. 89 (2016) 559–567.
[14] L. Wang, J. Xue, Q. Wang, Correlation between arc mode, microstructure, and mechanical properties during wire arc additive manufacturing of 316L stainless steel, Mater. Sci. Eng. A 751 (2019) 183–190.
[15] M. Dinovitzer, X. Chen, J. Laliberte, X. Huang, H. Frei, Effect of wire and arc additive manufacturing (WAAM) process parameters on bead geometry and microstructure, Addit. Manuf. 26 (2019) 138–146.
[16] C. Huang, P. Kyvelou, L. Gardner, Stress-strain curves for wire arc additively manufactured steels, Eng. Struct. 279 (2023) 115628, https://doi.org/10.1016/j.engstruct.2023.115628.
[17] Y. Lou, H. Huh, Extension of a shear-controlled ductile fracture model considering the stress triaxiality and the Lode parameter, Int. J. Solids Struct. 50 (2013) 447–455.
[18] Y. Bai, T. Wierzbicki, A new model of metal plasticity and fracture with pressure and Lode dependence, Int. J. Plast. 24 (2008) 1071–1096.
[19] Y. Bao, T. Wierzbicki, On fracture locus in the equivalent strain and stress triaxiality space, Int. J. Mech. Sci. 46 (2004) 81–98.
[20] C.C. Roth, D. Mohr, Effect of strain rate on ductile fracture initiation in advanced high strength steel sheets: experiments and modeling, Int. J. Plast. 56 (2014) 19–44.
[21] J.R. Rice, D.M. Tracey, On the ductile enlargement of voids in triaxial stress fields, J. Mech. Phys. Solids 17 (1969) 201–217.
[22] A.L. Gurson, Continuum Theory of Ductile Rupture by Void Nucleation and Growth: Part I—Yield Criteria and Flow Rules for Porous Ductile Media 99, 1977, pp. 2–15.
[23] V. Tvergaard, Influence of voids on shear band instabilities under plane strain conditions, Int. J. Fract. 17 (1981) 389–407.
[24] K. Nahshon, J.W. Hutchinson, Modification of the Gurson model for shear failure, Eur. J. Mech. A Solids 27 (2008) 1.
[25] L. Xue, Constitutive modeling of void shearing effect in ductile fracture of porous materials, Eng. Fract. Mech. 75 (2008) 3343–3366.
[26] Haohui Xin, Gao Liu, Youyou Zhang, Xiao Guo, Jie Li, Milan Veljkovic, Discussion on ultimate resistance formulas of high-strength bolts under tensile-shear coupling loading, J. Constr. Steel Res. 220 (2024) 108848.
[27] H. Xin, Recent progress in computational predictions on fatigue and fracture resistance of steel connection joints, Ce/Papers 6 (2023) 2550–2557, https://doi.org/10.1002/cepa.2658.
[28] E. ASTM, Standard test methods for tension testing of metallic materials, in: Annu. B. ASTM Stand, ASTM, 2001.
[29] H. Xin, J.A.F.O. Correia, M. Veljkovic, F. Berto, Fracture parameters calibration and validation for the high strength steel based on the mesoscale failure index, Theor. Appl. Fract. Mech. 112 (2021) 102929.
[30] F.B. Haohui Xin, Milan Veljkovic, José A.F.O. Correia, Ductile fracture locus identification using mesoscale critical equivalent plastic strain, Fatigue Fract. Eng. Mater. Struct. 1–13 (2021).
[31] ISO 636:2017, Welding Consumables — Rods, Wires and Deposits for Tungsten Inert Gas Welding of Non-Alloy and Fine-Grain Steels — Classification, ISO/TC 44/SC 3 Weld. Consum, 2017.
[32] H. Xin, M. Veljković, Evaluation of high strength steels fracture based on uniaxial stress-strain curves, Eng. Fail. Anal. 120 (2021) 105025.
[33] Y. Ling, Uniaxial true stress-strain after necking, AMP J. Technol. 5 (1996) 37–48.
[34] H. Xin, W. Sun, J. Fish, A surrogate modeling approach for additive-manufactured materials, Int. J. Multiscale Comput. Eng. 15 (2017) 525–543, https://doi.org/10.1615/IntJMultCompEng.2017024632.
[35] A. Needleman, Void Growth and Coalescence in Porous 24, 1988, pp. 835–853.
[36] J. Li, H. Xin, J.A.F.O. Correia, F. Berto, B. Zhao, Y. Bo, M. Veljkovic, Mesh size effects on fracture locus of high strength bolts: a mesoscale critical equivalent plastic strain (MCEPS) approach, Eng. Fail. Anal. 138 (2022), https://doi.org/10.1016/j.engfailanal.2022.106385.
[37] J. Fish, Practical Multiscaling, 2013.
[38] Y. Lou, J.W. Yoon, H. Huh, Modeling of shear ductile fracture considering a changeable cut-off value for stress triaxiality, Int. J. Plast. 54 (2014) 56–80.
[39] V. Abaqus, 2021 Documentation 651, Dassault Syst. Simulia Corp., 2021.